BARREL-STAVE FLEXTENSIONAL TRANSDUCER DESIGN

A THESIS
SUBMITTED TO THE DEPARTMENT OF ELECTRICAL AND ELECTRONICS ENGINEERING
AND THE INSTITUTE OF ENGINEERING AND SCIENCES
OF BILKENT UNIVERSITY
IN PARTIAL FULLFILMENT OF THE REQUIREMENTS
FOR THE DEGREE OF
MASTER OF SCIENCE

By
Aykut Şahin
March 2009

I certify that I have read this thesis and that in my opinion it is fully adequate, in scope and in quality, as a thesis for the degree of Master of Science.

Prof. Dr. Hayrettin Köymen (Supervisor)

I certify that I have read this thesis and that in my opinion it is fully adequate, in scope and in quality, as a thesis for the degree of Master of Science.

Prof. Dr. Yusuf Ziya İder

I certify that I have read this thesis and that in my opinion it is fully adequate, in scope and in quality, as a thesis for the degree of Master of Science.

Assoc. Prof. Dr. Tolga Çiloğlu

Approved for the Institute of Engineering and Sciences:

Prof. Dr. Mehmet B. Baray
Director of Institute of Engineering and Sciences

ABSTRACT

BARREL-STAVE FLEXTENSIONAL TRANSDUCER DESIGN

Aykut Şahin
M.S. in Electrical and Electronics Engineering
Supervisor: Prof. Dr. Hayrettin Köymen
March 2009

This thesis describes the design of low frequency, high power capability class-I flextensional, otherwise known as the barrel-stave, flextensional transducer. Piezoelectric ceramic rings are inserted inside the shell. Under an electric drive, ceramic rings vibrate in the thickness mode in the longitudinal axis. The longitudinal vibration of the rings is transmitted to the shell and converted into a flexural motion. Low amplitude displacements on its axis create high total displacement on the shell, acting as a mechanical transformer.

Equivalent circuit analysis of transducer is performed in MATLAB and the effects of structural variables on the resonance frequency are investigated. Critical analysis of the transducer is performed using finite element modeling (FEM). Three dimensional transducer structure is modeled in ANSYS, and underwater acoustical performance is investigated. Acoustical analysis is performed by applying a voltage on piezoelectric material both in vacuum and in water for the convex shape barrel-stave transducer. Effects of transducer structural variables, such as transducer dimensions, shell thickness, shell curvature and shell material, on the electrical input impedance, electro-acoustical transfer function, resonance frequency and quality factor are investigated. Thermal analysis of designed transducer is performed in finite element analysis. Measured results of the transducer are compared with the theoretical results.

Keywords: Underwater Acoustic Transducer, Barrel-Stave, Flextensional Transducer, Low Frequency, High Power, Piezoelectric.

ÖZET

1. SINIF GERİLİM İLE BÜKÜLEN AKUSTİK DÖNÜŞTÜRÜCÜ TASARIMI

Aykut Şahin
Elektrik ve Elektronik Mühendisliği Bölümü Yüksek Lisans
Tez Yöneticisi: Prof. Dr. Hayrettin Köymen
Mart 2009

Bu tezde düşük frekanslarda yüksek güç gerektiren uygulamalara uygun 1. Sınıf fıçı tipi, gerilim ile bükülen (Barrel-stave flextensional) akustik dönüştürücü tasarımı tartışılmaktadır. Fıçı tipi dönüştürücünün iç kısmında halka tipi piezoelektrik malzeme bulunmaktadır. Bu piezoelektrik malzemeye elektriksel gerilim uygulanmakta ve piezoelektrik malzemede boylamsal hareket oluşturulmaktadır. Fıçının orta kısmında oluşan boylamsal hareketler kabuk kısmında bükülmelere neden olmaktadır. Bu şekilde fıçı mekanik bir transformatör etkisi göstererek eksenindeki küçük genlikli titreşimleri geniş fıçı yüzeyi marifeti ile ortama yükselterek aktarmaktadır.

Fıçı dönüştürücü eşdeğer devre çözümlemesi MATLAB programı ile gerçekleştirilmiş ve fıçı parametrelerinin rezonans frekansı üzerindeki etkileri incelenmiştir. Fıçının kritik analiz çözümlemeleri sonlu eleman modelleme (Finite Element Model: FEM) yöntemi kullanılarak gerçekleştirilmiştir. ANSYS programında, fıçı, su içerisinde üç boyutlu modellenerek akustik performansı incelenmiştir. Akustik analizler piezoelektrik malzemeye gerilim uygulayarak, boşlukta ve suda dışbükey fıçı tipi dönüştürücü için gerçekleştirilmiştir. Fıçı boyutları, kabuk kalınlığı ve eğriliği, kabuk malzemesi gibi fıçının yapısal parametrelerinin, dönüştürücünün elektriksel giriş empedansı, elektro-akustik transfer fonksiyonu, rezonans frekansı, kalite faktörü üzerindeki etkileri incelenmiştir. Tasarlanan dönüştürücü ısıl analizleri sonlu eleman modellemesi

ile gerçekleştirilmiştir. Dönüştürücü ölçüm sonuçları teorik sonuçlar ile karşılaştırılmıştır.

Anahtar Kelimeler: Sualtı Akustik Dönüştürücü, Barrel-Stave, Flextensional Transducer, Düşük Frekans, Yüksek Güç, Piezoelektrik

To my parents and my fiance…

Acknowledgements

I would like to express my gratitude to my supervisor Prof. Dr. Hayrettin Köymen for his instructive comments and guidance in the supervision of the thesis. I would also like to express my special thanks to the jury members Prof. Dr. Y. Ziya İder and Assoc. Prof. Dr. Tolga Çiloğlu for evaluating my thesis.

I would like to thank Zekeriyya Şahin, Sacit Yılmaz, and H. Kağan Oğuz for providing valuable discussions and their support. I would like to thank A. Gözde Ulu and other employees of ASELSAN who worked on the construction of barrel-stave transducer.

I would like to express my gratitude to Prof. Dr. Aydın Doğan for his valuable support in the production of alumina rings. I would also like to thank to Dr. D.T.I. Francis for his kind and valuable help for overcoming the problem in the modeling of transducer in ANSYS.

I would also like to express my thanks to my parents Bilal-Münevver Şahin, my fiancé Özlem, and my sister and her family Aysun-Kemal-Ela Özkan for their support and endless love throughout my life.

Finally, special thanks to the TUBITAK for its' valuable financial support.

Table of Contents

List of Figures

List of Tables

Chapter 1

Introduction

Medium exhibits very different characteristics compared to air in terms of propagation. Strong conductivity of salt water makes the water medium dissipative for electromagnetic waves which means that their attenuation is rapid, and their range is limited [1].

Acoustic waves are the only way today to carry information from one point to another inside the water medium. Engineering science of sonar, acronym of sound navigation and ranging, deals with the propagation of sound in water. Sound propagation in active sonar systems is two-way that start from the generation of sound by projector, which creates sound pressure waves according to the applied electrical signals, and ending by the reception of echoes by hydrophone, which converts incoming sound waves into electrical signals. In passive sonar systems there is one-way propagation and the system listens the sound radiated by the target using hydrophones [2].

There is a significant difference between the power handling limits of projectors and hydrophones. Projectors are used as high power acoustic sources, so their power handling levels are high, whereas power-handling levels of hydrophones are low [3]. Therefore, due to the high power handling requirements, projectors have more challenging design needs, and in this thesis the design of barrel-stave flextensional projector is handled.

In the first chapter, we first give some historical background basically on acoustics, and then we briefly discuss the application areas of acoustics in

military and civilian applications. Next, we discuss the piezoelectric effect, piezoelectric materials and their properties. Afterwards, we explain the Finite Element Modeling (FEM), which is used very often in transducer design. Then, we describe the analogy between electromagnetic and acoustic waves. Finally, we define the parameters used to define the transducer acoustical properties.

In the second chapter, we discuss the classification schemes and application areas of barrel-stave transducer. Then, we summarize the related works on barrel-stave transducers.

Third chapter deals with the equivalent circuit representation of barrel-stave transducer. Firstly, we mention the basic equivalent circuit theory, and then we describe the equivalent circuit model for the barrel-stave flextensional transducer.

In the fourth chapter, we analyze the performance of barrel-stave transducer equivalent circuit using the known structural parameter set and its FEM results. Then, we compare the equivalent circuit and FEM results.

We will focus on the modeling and analysis of barrel-stave flextensional transducer in ANSYS in the fifth chapter. First, we explain the modeling of barrel-stave transducer in ANSYS. Then, we discuss the design of barrel-stave transducer using FEM in ANSYS. Lastly, we make some correction on some elements of the transducer equivalent circuit model of transducer using FEM results.

In the sixth chapter, we analyze the power limitations of barrel-stave flextensional transducer in terms of electrical limitations, cavitation limitations, and thermal limitations.

In the seventh chapter, we describe the construction and measurement of the designed transducer. First, we explain the steps and details of construction process. Then, we measure the constructed transducer both in vacuum and water.

1.1 History of Underwater Acoustics

One of the earliest references of the existence of sound at sea is from the notebooks of the Leonardo da Vinci at the last quarter of 15th century. The first quantitative measurement in underwater and sound occurred by the Swiss physicist, Daniel Colladon, and French mathematician, Charles Sturm, in 1827 where they measure the velocity of sound [2].

In the 1840s, James Joule discovered the effect of magnetostriction [2]. In 1880, Jacques and Pierre Curie discovered piezoelectricity in quartz and other crystals. The discoveries of these magnetostriction and piezoelectricity, which are still used in most underwater transducers, have tremendous significance for underwater sound [4].

In 1912, R.A. Fessenden developed a new type of moving coil transducer, which was successfully used for signaling between submarines and for echo ranging by 1914 [4].

At the beginning of World War II, active sonar system technology was improved enough to be used by the Allied navies [1].

After the World War II, active sonars have grown larger and more powerful and operate at frequencies several octaves lower than in World War II. Therefore, the active sonar ranges improves to greater distances. In order to increase the effective range of the passive sonar systems, their operational

frequencies decreased, which allows taking the advantage of the low frequency ship noise of the submarines. However, at the same time the submarines have become quiter, and have become far more difficult targets for passive detection than before [2].

1.2 Underwater Acoustic Applications

Underwater acoustic technology is used in scientific, military and industrial areas.

Most military underwater acoustic applications aimed at detecting, locating, and identifying of targets. Depending on their functionality, military sonars are classified into two categories [1];

Active sonars, which transmits and receives echoes returning from the target.

Passive sonars which intercepts noises and active sonar signals radiated by target.

Civilian applications are developed to meet the needs of scientific programmes of environment study and monitoring, as well as the offshore engineering and fishing. The main categories of civilian applications are as follows [1];

Bathymetric sounders that measure the water depth.

Fishery sounders designed for the detection and localization of fish shoals.

Sidescan sonars used for the acoustic imaging of the seabed.

Multibeam sounders used for seafloor mapping.

Sediment profilers used for the study of internal structure of the seabed.

Acoustic communication systems used as a telephone link and for the transmission of digital data.

Positioning systems used to find the position of platforms.

Acoustic Doppler system used to measure the speed of sonar relative to fixed medium, or the speed of water relative to a fixed instrument using the frequency shift.

Acoustic tomography systems used to assess the structure of hydrological perturbations.

1.3 Piezoelectric Effect

Jacques and Pierre Curie discovered piezoelectric effect in 1880. The name is made up of two parts; piezo, which is derived from the Greek word for pressure, and electric from electricity [5]. Literally, it means pressure - electric.

In a piezoelectric material, generation of electrical charge by the application of mechanical force is called the direct piezoelectric effect. Conversely, creating a change in mechanical dimensions by the application of charge is called the inverse piezoelectric effect.

Several ceramic materials such as lead-zirconate-titanate (PZT), lead-titanate (PbTiO2), lead-zirconate (PbZrO3), and barium-titanate (BaTiO3) have been described as exhibiting a piezoelectric effect [5].

Ceramic material is made up of large numbers of randomly orientated crystal grains. The ceramic material does not exhibit a piezoelectric effect in a randomly oriented condition. Therefore, the ceramic must be polarized.

The ceramic materials are heated above a certain temperature called Curie point and applied a high direct electric field. Under a strong and steady electric field orientation of crystal grains partially aligned. Cooling the ceramic below its curie point first and removing the electric field results in a remanent

polarization in ceramic material. In this polarized ceramic materials, in other words piezoelectric materials there is a linear relation between the electrical field and mechanical strain [4].

Linear relation between the electrical and mechanical behavior of the piezoelectric materials is described as a set of linear tensor equations that relate stress, T, strain, S, electric field, E, and electric displacement, D as follows [6]:

$$\{T\} = \left[c^E \right]\{S\} - [e]\{E\} \tag{1.1}$$

$$\{D\} = [e]^T \{S\} + \left[\varepsilon^S \right]\{E\} \tag{1.2}$$

$\left[c^E \right]$: 6 x 6 symmetric matrix specifies the stiffness coefficients

$$[c] = \begin{array}{c} \\ x \\ y \\ z \\ xy \\ yz \\ xz \end{array} \begin{array}{c} \begin{array}{cccccc} x & y & z & xy & yz & xz \end{array} \\ \begin{bmatrix} c_{11} & c_{12} & c_{13} & c_{14} & c_{15} & c_{16} \\ & c_{22} & c_{23} & c_{24} & c_{25} & c_{26} \\ & & c_{33} & c_{34} & c_{35} & c_{36} \\ & & & c_{44} & c_{45} & c_{46} \\ & & & & c_{55} & c_{56} \\ & & & & & c_{66} \end{bmatrix} \end{array}$$

$[e]$: 6 x 3 symmetric matrix specifies the piezoelectric stress matrix

$$[e] = \begin{array}{c} \\ x \\ y \\ z \\ xy \\ yz \\ xz \end{array} \begin{array}{c} \begin{array}{ccc} x & y & z \end{array} \\ \begin{bmatrix} e_{11} & e_{12} & e_{13} \\ e_{21} & e_{22} & e_{23} \\ e_{31} & e_{32} & e_{33} \\ e_{41} & e_{42} & e_{43} \\ e_{51} & e_{52} & e_{53} \\ e_{61} & e_{62} & e_{63} \end{bmatrix} \end{array}$$

$\left[\varepsilon^S\right]$: 3 x 3 dielectric matrix

$$\left[\varepsilon^S\right] = \begin{bmatrix} \varepsilon_{11} & 0 & 0 \\ 0 & \varepsilon_{22} & 0 \\ 0 & 0 & \varepsilon_{33} \end{bmatrix}$$

General Comparison of Piezoelectric Ceramics

Ceramic-B is a modified barium titanate, which offers improved temperature stability and lower aging in comparison with unmodified barium titanate.

PZT-4 is recommended for high power acoustic radiating transducers because of its high resistance to depolarization and low dielectric losses under high electric drive. Its high resistance to depolarization under mechanical stress makes it suitable for use in deep-submersion acoustic transducers and as the active element in electrical power generating systems.

PZT-5A is recommended for hydrophones or instrument applications because of its high resistivity at elevated temperatures, high sensitivity, and high time stability.

PZT-8 is similar to PZT-4, but has even lower dielectric and mechanical losses under high electric drive. It is recommended for applications requiring higher power handling capability than is suitable for PZT-4.

Military specification for classifies ceramics into four basic types [7],

Type I (PZT-4)

Hard lead zirconate-titanate with a Curie temperature equal to or greater than 310ºC

Type II (PZT-5A)

Soft lead zirconate-titanate with a Curie temperature equal to or greater than 330ºC

Type III (PZT-8)

Very hard lead zirconate-titanate with a Curie temperature equal to or greater than 330ºC

Type IV (Ceramic-B)

Barium titanate with nominal additives of 5 percent calcium titanate and 0.5 percent cobalt carbonate as necessary to obtain a Curie temperature equal to or greater than 100ºC

The terms ‘hard’ and ‘soft’ refer to the composition type. Hard materials are not easily poled or de-poled except at elevated temperatures which make these materials suitable for projector that operate at high power levels. Soft materials are more easily poled or de-poled. They have high electro-mechanical coupling coefficients, which makes these materials suitable for hydrophones, or low power projectors.

1.4 Finite Element Method (FEM)

Finite element method first appeared in 1960, when it was used in a paper on plane elasticity problems. In the years since 1960 the finite element method has received widespread acceptance in engineering [8].

Many problems can be solved approximately using a numerical analysis technique called the finite element method.

In the finite element method the problem is reduced to a finite element unknown problem by dividing the structure into a finite number of smaller sub

regions or finite elements. The 'coarseness' of these elements determines the accuracy of the solution. Therefore, as the number of elements increases approximation to the actual solution improves [7].

Applying an approximation function (interpolation function) within each element, the actual infinite number of unknown problem can be well transformed into a finite element problem [7, 8]. Each field variable is defined at specific points on structure called nodes. The nodal values of the field variable and the interpolation functions for the elements completely define the behavior of the field variable within the elements [8].

In practice, a finite element analysis usually consists of three principal steps [9]:

Preprocessing: Model construction part
Analysis: Constructed model is solved
Postprocessing: Examining the solution

For harmonic vibration at a frequency w, in radians per second the finite element equation becomes [7, 10]:

$$\left[-w^2\left[M\right]+\left[K\right]\right]\left\{u_n\right\}=\left\{F\right\} \tag{1.3}$$

where [M] is the mass matrix, [K] is the stiffness matrix, and {F} is the electromechanical forcing function.

The solution set is obtained by solving the above equation on each node.

1.5 Electrical Analogs of Acoustical Quantities

Electrical equivalent circuits are extensively used in the representation of transducers. In equivalent circuit model of transducers voltage, V, and current, I, are used to represent the force, F, and velocity, u and lumped electrical elements such as resistors, inductors and capacitors are used to represent the resistance, mass and compliance (1/stiffness) respectively [4].

This analogy originates from the similarities of the electrical and magnetic equations shown in Table 1 [4].

1	Electrical Resistance	$V = R_e I$
	Mechanical Resistance	$F = Ru$
2	Inductance	$V = jwLI$
	Mass	$F = jwMu$
3	Capacitor	$V = I/jwC$
	Compliance (1/Stiffness)	$F = u/jwC_m$
4	Electrical Power	$P = VI$
	Mechanical Power	$P = Fu$

Table 1 Analogy between the electrical and mechanical equations

Therefore, vibrating mechanical system can be represented by the replacement of mechanical and electrical quantities as shown in Table 2.

Mechanical	**Electrical**
F	V
u	I
C_m ($1/K_m$)	C
M	L

Table 2 Analogy between the electrical and mechanical parameters

1.6 Basic Transducer Parameters

Some definitions and formulas related to the transducers and hydrophones are listed below;

1. Directivity Index [2]:

$$DI_T = 10\log_{10}\left(\frac{I_D}{I_{Nond}}\right) \tag{1.4}$$

where T emphasizes that the transmitting directivity index

$I_{D:}$ Directional pattern intensity

$I_{Nond:}$ Nondirectional pattern intensity

2. Source Level or Source Pressure Level [3, 11]:

Sound pressure (acoustic power) in dB referenced to 1.0 μPa measured at 1meter from the sound source.

$$SL = 10\log_{10}\left(\frac{Intensity\,of\ source}{reference\,\text{int}ensity\ (1\mu Pa)}\right) \tag{1.5}$$

$$SL(dB\,re\,1\mu Pa) = 170.9 + 10\log_{10}\left(radiated\ power\left(P_r\right)\right) + DI_T \tag{1.6}$$

Source level can also be defined as pressure level referenced to 1.0 μPa in dB scale as;

$$SL(dB\,re\,1\mu Pa) = 20\log_{10}\left(\frac{p_{rms}}{p_{ref}}\right) \tag{1.7}$$

3. Transmitting Voltage Response [11]:

Transmitting Voltage Response (TVR) is the pressure level at 1m range per 1 V of input voltage as a function of frequency.

4. Sensitivity [2]:

Hydrophone sensitivity is given in dB referenced to 1 Volt/μPa (dB re 1 V/μPa)

5. Beam Width [2]:

The width of the main beam lobe, in degrees, of the transducer. It is usually defined as the width between the "half power point" or "-3dB" point.

6. Efficiency [2]:

In a projector, efficiency is defined as the ratio of the acoustic power generated to the total electrical power input. Efficiency varies with frequency and is expressed as a percentage.

7. Quality Factor [2]:

$$Q = \frac{f_0}{f_2 - f_1} \tag{1.8}$$

where f_0 : Resonance Frequency

(f_2-f_1) : Bandwidth

Chapter 2

Barrel-Stave Transducers

Throughout this chapter, the classification schemes of flextensional transducers and the application areas of barrel-stave flextensional transducers are discussed. In addition, we have summarized the previous works on barrel-stave transducers.

We have divided this chapter into three sections. Two different classification schemes of flextensional transducers that are the Pagliarini-White scheme and the Brigham-Royster scheme are clarified in section 2.1. In section 2.2 the application areas of barrel-stave transducers and the advantages of barrel-stave transducers compared to others in low frequency and high power applications are mentioned. In section 2.3, the previous works on the design of barrel-stave transducer are analyzed.

2.1 Flextensional Transducer Classification Schemes

There are two classification schemes for the flextensional transducers, one is the Pagliarini-White classification scheme and the other is the Brigham-Royster classification scheme.

The criteria that is used to distinguish the four classes defined in Pagliarini-White scheme, as shown in Figure 1, is based on shape [7, 12].

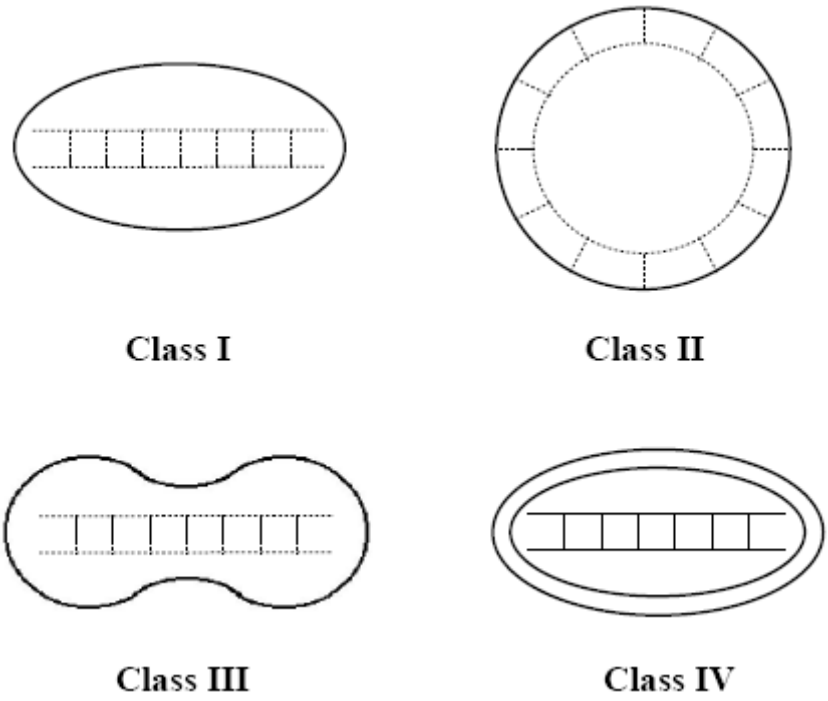

Figure 1 The Pagliarini-White classification scheme

In Brigham-Royster scheme, as shown in Figure 2, more complex method is used. Classes I, IV, V are distinguished by shell shape. However, classes I, II, and III are distinguished by pragmatic criteria; class II is a high power version of class I and class III is a broadband version of class I [7, 12]. In this classification scheme, the class-I flextensional type transducer is also known as the barrel-stave flextensional transducer.

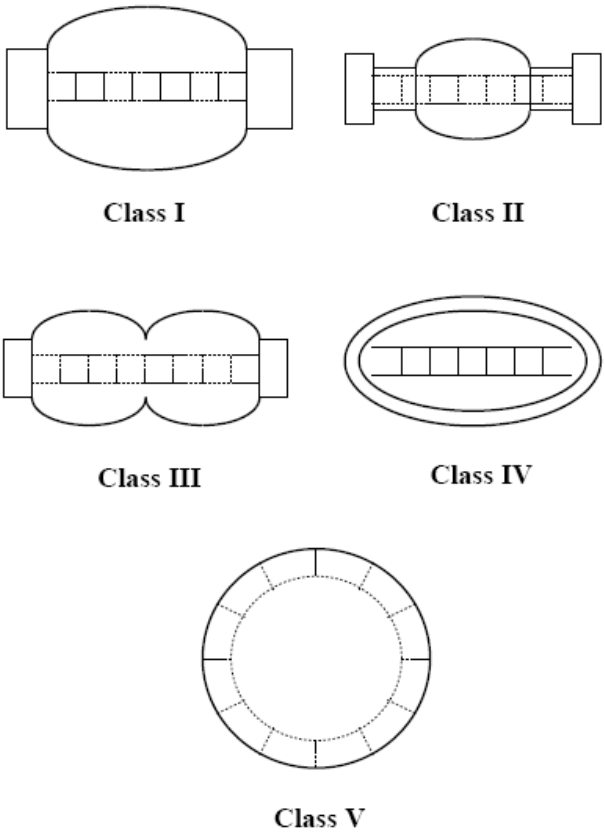

Figure 2 The Brigham-Royster classification scheme

2.2 Application Areas of Barrel-Stave Transducers

In sonar and oceanography applications, the design of low frequency, high power, underwater acoustic projectors have a high propriety.

New technology ship designs reduce the own ship noise of submarines, so the usefulness of the passive towed arrays has been substantially diminished. Thus long-range detection in underwater applications can now only be made by using low-frequency active sonar systems [13].

In oceanography applications, low frequency projectors have been used to track the deep oceanic water circulations, calculate the sound speed in water, and communicate with the offshore systems [13].

Barrel-stave transducers are used in vertical array arrangements to improve the horizontal directivity, and reduce the unwanted acoustic energy transmission to the ocean floor and to the sea surface [14].

2.3 Barrel-Stave Transducers

The barrel-stave transducer consists of a piezoelectric stack and a surrounding mechanical shell that is cylindrical. The mechanical shell has slots along the axial z-direction in order to reduce the axial stiffness and decrease the resonance frequency of the transducer. Under an electric drive, the ceramic stack vibrates in the thickness mode in the longitudinal axis, which results in the end plates extend in the axial direction. The axial vibration of the end plates is transmitted to the shell and converted into a flexural motion.

The equivalent circuit of the barrel-stave transducer, which is described by the modified Brigham's equivalent circuit model, demonstrates the mechanical characteristics of transducer in electrical circuit form [15]. Detailed description of the equivalent circuit is given in chapter 3.

Although it provides reliable results, many assumptions have made during the equivalent circuit analysis. Finite Element Analysis has made to see the effects of the ignored parameters on the performance of the transducer.

D.T.I. Francis has investigated the effects of the structural parameters on the performance of the transducer in FEA [14].

In Clive Bayliss's doctorate thesis, he has also investigated the effects of the structural parameters on the performance of the transducer in FEA. He has compared the measured results with the theoretical results obtained by FEA and found that they are consistent [7].

Soon Suck Jarng compares the barrel-stave sonar transducer simulation between a coupled FE-BEM and ATILA, which has a BEM (Boundary Element Method) solver and found that FE-BEM results agree well with the ATILA results.

In the following chapters, the design of barrel-stave transducer using both the equivalent circuit and FEA is explained. We use MATLAB for the equivalent circuit analysis and ANSYS for the FEA.

Chapter 3

Equivalent Circuit Representation

Using the analogy between the electrical and mechanical systems, mechanical systems such as transducers can be represented by an electrical equivalent circuit. Electrical equivalent circuit analysis provides powerful insight on the effects of each design parameters to the performance of transducer.

Using this analogy, theory of the basic transducer equivalent circuit modeling is mentioned in section 3.1. Derivation of equivalent circuit of transducer describes methods of how the mechanical parameters of transducer are represented by their electrical analogs. Section 3.2 describes the modified Brigham's equivalent circuit for the barrel-stave flextensional transducer.

3.1 Basic Transducer Equivalent Circuit Theory

Piezoelectric transducers can be represented by a 4-terminal network as illustrated in Figure 3.

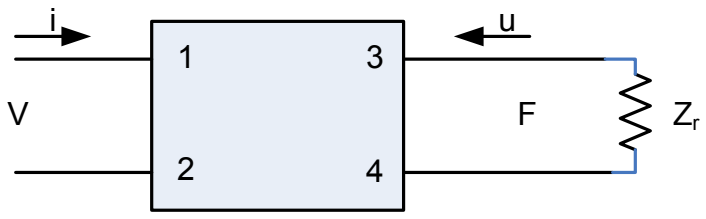

Figure 3 4-terminal representation of transducer

First and second terminals shown in Figure 3 represent the input electrical terminals, whereas third and fourth terminals represent the output mechanical terminals [3].

When an alternating voltage V is applied to the input terminals, by piezoelectric behavior of the transducer, alternating force F is generated at the output terminals. In this case the radiation impedance Z_r of transducer can be formulated as follows;

$$Z_r = \frac{F}{-u} \tag{3.1}$$

As a consequence of the reciprocal nature of the transducer, when an alternating force F is applied to the output terminals, alternating voltage V is generated at the input terminals. Therefore, transducer behaves as a transformer that converts between electrical and mechanical quantities with a transformation ratio N [3].

When transducer is in the radiation state into Z_r, the input current of the transducer in terms of the applied input voltage V is formulated as follows;

$$i = Y_e V - Nu \tag{3.2}$$

where Y_e is the blocked electrical input impedance. In piezoelectric transducers Y_e is the parallel combination of the clamped capacitance C_0 and the dielectric loss resistance R_e.

If an alternating force F is applied to the mechanical terminals, the relation between the force and the displacement u is formulated as follows;

$$F = NV + Z_m u \tag{3.3}$$

where Z_m is the mechanical impedance at the mechanical terminals when $V = 0$.

Combination of the equations in (3.1), (3.2), and (3.3) gives an electrical input current as;

$$i = Y_e V + \frac{N^2 V}{Z_m + Z_r} \tag{3.4}$$

So the input impedance Y_{in} is;

$$Y_{in} = Y_e + \frac{N^2 V}{Z_m + Z_r} \tag{3.5}$$

The mechanical impedance Z_m of a transducer is the series combination of the mechanical compliance C_m, which is the inverse of the effective stiffness K, effective vibrating mass M, and the mechanical loss resistance R_m as illustrated below [3];

$$Z_m = R_m + jwM + \frac{1}{jwC_m} \tag{3.6}$$

Using the above circuit element expressions, piezoelectric transducer's equivalent circuit model is obtained as shown in Figure 4.

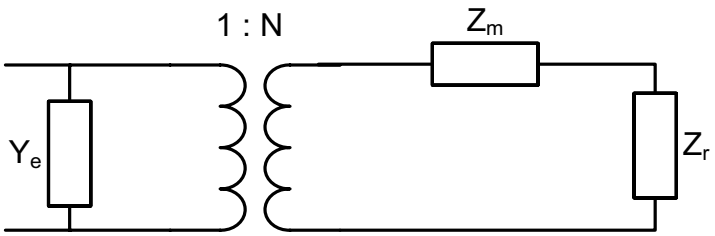

Figure 4 Piezoelectric transducer's general equivalent circuit

3.2 An Equivalent Circuit Model for Barrel-Stave Flextensional Transducer

Equivalent circuit model of barrel-stave flextensional transducer is shown in Figure 5 [15].

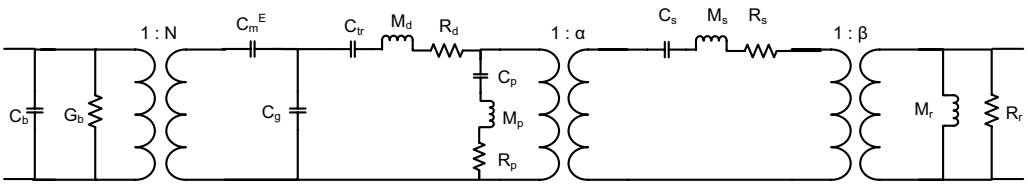

Figure 5 Equivalent circuit model of barrel-stave flextensional transducer

In piezoelectric driver side C_b is the blocked capacitance of the piezoelectric rings driven in 33 mode, G_b is the electrical loss conductance of piezoelectric rings, N is the electromechanical transformation ratio, C_m^E is the short circuit compliance of the rings, C_g is the adhesive joints between the rings, C_{tr} is the center bolt compliance, M_d is the driver mass, R_d is the driver loss factor.

In the mechanical side of staves, C_p, M_p, and R_p represent the higher frequency extensional mode compliance, mass, loss resistance, respectively, of

staves. α represents the transformation of axial motion on either side of staves to the radial motion. C_s, M_s, and R_s represent the fundamental flexural mode compliance, mass, loss resistance, respectively, of staves. β is the transformation of rms displacement to average displacement on staves in the radial direction where rms and average displacements are calculated as;

$$\xi_{rms} = \sqrt{\frac{1}{n}\sum_{1}^{n}\xi_i^2} \tag{3.7}$$

$$\xi_{average} = \frac{1}{n}\sum_{i=1}^{n}\xi_i \tag{3.8}$$

M_r and R_r are the radiation mass and radiation resistance of transducer, respectively.

The piezoelectric driver side equivalent circuit element formulations are;

$$C_b = n^2 \varepsilon_{33}^S A / l \tag{3.9}$$

$$G_b = wC_b \tan\delta_e \tag{3.10}$$

$$N = nd_{33}Y_{33}^E A / l \tag{3.11}$$

$$C_m^E = l / Y_{33}^E A \tag{3.12}$$

$$C_g = (n+1)l_g / Y_g A \tag{3.13}$$

$$R_d = \tan\delta_d / w(C_m^E + C_g) \tag{3.14}$$

$$C_{tr} = l_{tr} / Y_{tr} A_{tr} \tag{3.15}$$

$$M_d = M_h M_t / (M_h + M_t) \tag{3.16}$$

where n is the number of rings in the piezoelectric stack, ε_{33}^S is the blocked permittivity, l is the stack length (along the transducer axis), A is the stack cross sectional area, $\tan\delta_e$ is the electrical loss factor, w is the angular

frequency, d_{33} is the piezoelectric constant, Y_{33}^{E} is the short circuit Young's modulus of the piezoelectric material, l_g is the bond thickness, Y_g is the adhesive modulus, $\tan\delta_d$ is the driver loss factor, l_{tr} is the center bolt length, Y_{tr} is the center bolt Young's modulus, A_{tr} is the center bolt cross-sectional area.

In the driver mass, M_d, equation, M_h is the corrected head mass, and M_t is the corrected tail mass where they are the combinations of the ring-stack and end masses expressed as follows:

$$M_h = m_h + \rho Al/3\phi \tag{3.17}$$

$$M_t = m_t + \rho Al(\phi - 1)/3\phi \tag{3.18}$$

where ρ is the piezoelectric density, m_h and m_t are the actual head and tail masses, respectively, and ϕ is

$$\phi = (m_h + m_t + 2\rho Al/3)/(m_t + \rho Al/3) \tag{3.19}$$

The stave mechanics side equivalent circuit element formulations are;

$$C_p = l_s / vY_s bh \tag{3.20}$$

$$R_p = \tan\delta_p / wC_p \tag{3.21}$$

$$M_p = v\rho_s bhl_s(\phi - 1)/3\phi^2 \tag{3.22}$$

$$\alpha \cong 0.83(1 + 0.14l_s / r)l_s / r \tag{3.23}$$

$$M_s = v\rho_s bhl_s \tag{3.24}$$

$$C_s = 0.024(l_s / h)^3 / vY_s b \tag{3.25}$$

$$R_s = \tan\delta_s / wC_s \tag{3.26}$$

$$\beta = 1.2 \tag{3.27}$$

$$M_r = \pi\rho_0 (dl_s)^{3/2} / 2 \tag{3.28}$$

$$R_r = \pi dl_s \rho_0 c_0 \tag{3.29}$$

where l_s is the unsupported stave length, b is an average stave width, h is an average stave thickness, v is the number of staves, Y_s is the stave material Young's modulus, ρ_s is the stave material density, and $\tan\delta_p$ is a loss factor for the higher mode, r is the radius of curvature, $\tan\delta_s$ is the stave loss factor, ρ_0 is the water density, c_0 is the sound speed in water medium, and d is the mean diameter of the radiating surface ($d \cong vb/\pi$).

Barrel-stave flextensional transducers have two modes of operation in terms of the behavior of staves with the end masses. In equivalent circuit model, the C_p, M_p, and R_p resonator represents the higher frequency extensional mode, whereas the C_s, M_s, and R_s resonator (to which is added the radiation load of the water medium) represents the fundamental, flexural mode of the transducer. In fundamental, flexural mode of the transducer, all surfaces expand and contract in phase that means the end mass motion is in phase with the radial motion of the staves, whereas in higher frequency extensional mode of the transducer, end mass displacement and the stave radial displacements are out of phase.

The fundamental, flexural motion where the convex stave is displaced radially inward as the ends are stretched is shown in Figure 6 (a), whereas, the higher frequency, extensional motion where the convex stave bends, as the ends are stretched is shown in Figure 6 (b).

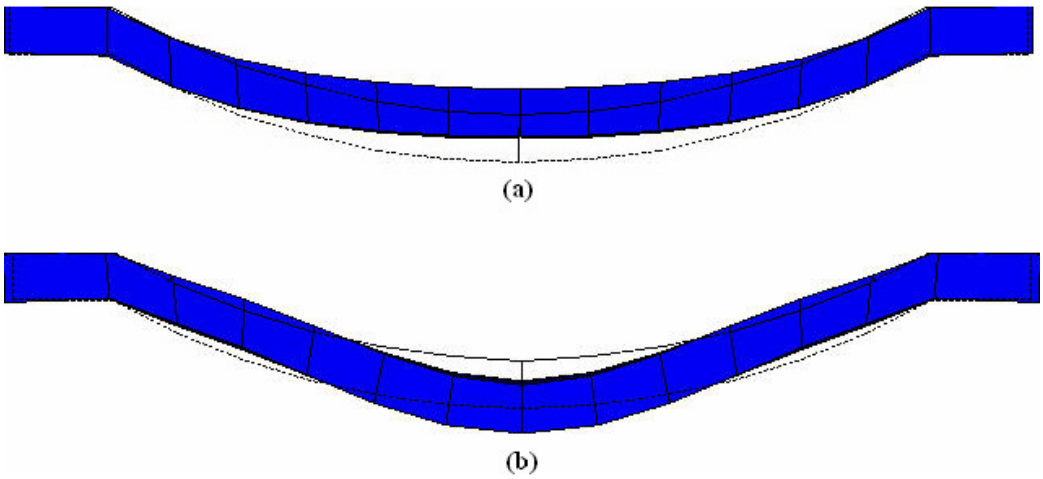

Figure 6 (a) Fundamental, flexural mode; (b) Higher frequency extensional, extensional mode. Dashed curve is undeformed stave shape.

Chapter 4

Design of Barrel-Stave Transducer Using Brigham's Equivalent Circuit Model

In chapter 3, the equivalent circuit representation of barrel-stave flextensional transducer is given. Some parameters of this equivalent circuit model is derived using the FEM results and includes some approximations.

Clive Bayliss founds that the mathematical analysis difficult and the optimization using the large number of variables complicated. Therefore, he carried out his work using the finite element and boundary element methods to design the barrel-stave flextensional transducer [7].

In this chapter, we compare the Brigham's modified equivalent circuit model results with the Clive Bayliss's results in order to determine the consistency between the equivalent circuit model and FEM.

4.1 Sample Equivalent Circuit Analysis

In Clive Bayliss's Thesis, there are some FEM results obtained from different designs. He has carried out his barrel-stave flextensional transducer design for both slotted-shell and staved-shell transducer types. In both types the

shell section consists of number of sections known as staves. In slotted-shell configuration the shell is circular in the hoop direction; however, in staved-shell configuration staves are curved in the axial direction but flat in the hoop direction. Slotted-shell and staved-shell structures are illustrated in Figure 7 and Figure 8, respectively.

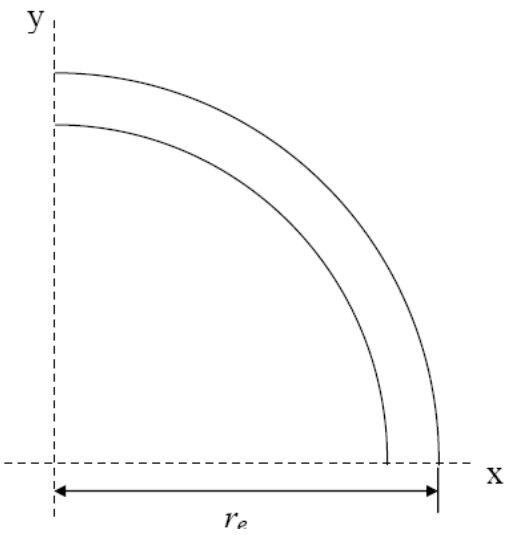

Figure 7 Slotted-Shell Transducer (top view)

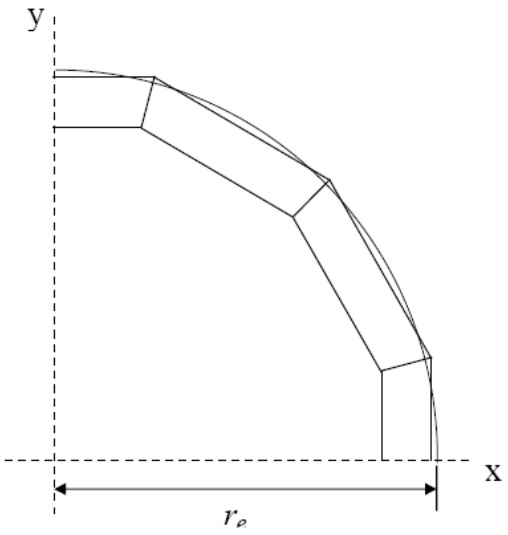

Figure 8 Staved-Shell Transducer (top view)

Staved-shell type has lower resonance frequency and lower acoustic power compared to the slotted-shell configuration. Our aim is to obtain the transducer with low resonance frequency, so we focus on the design of staved-shell flextensional transducer design.

The structural dimensions and the material properties that are used by Clive Bayliss are listed in Appendix I.

We used the material properties and the structural dimensions given in appendix I in the barrel-stave equivalent circuit. Young's modulus of PZT-4 rings, Y, depends on the sound speed inside the PZT-4 material, u, and density of PZT-4 material, ρ ,as;

$$Y = u^2 \rho \tag{4.1}$$

Assuming the sound speed as $u = 4000\, m/s$, Young's modulus of PZT-4 rings becomes $Y = 120.8\, GPa$.

Using the structural variables and Young's modulus as mentioned above, conductance and susceptance of transducer that is seen from the electrical terminals of the equivalent circuit is given in Figure 9.

The power that is transmitted into the transducer is directly proportional to the input conductance as;

$$P = \frac{1}{2}\left|\frac{V}{Z}\right|^2 R \tag{4.2}$$

Conductance curve gives the information about the power characteristics of the transducer as shown in Eq. 4.2. Therefore, conductance and susceptance graphs have high importance for estimating the performance of the transducer.

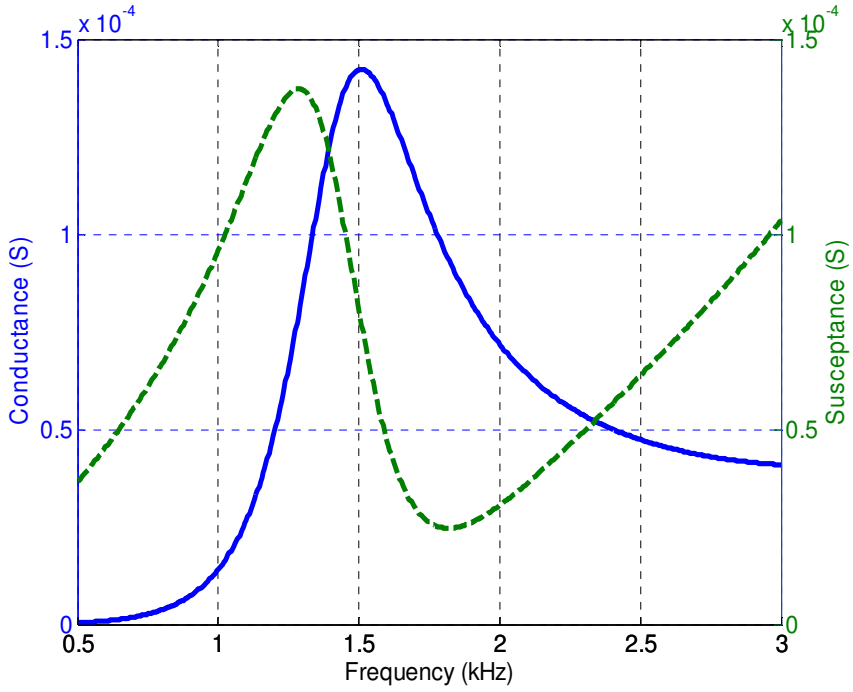

Figure 9 In-water conductance-susceptance seen from the electrical terminals obtained from equivalent circuit analysis

4.2 Comparison of Equivalent Circuit Results and FEM Results

Clive Bayliss has calculated the in water performance of the transducer using the same physical parameters and material orientations as in our equivalent circuit analysis using the FEM method. Bayliss found the fundamental resonance frequency of the transducer as 925 Hz and bandwidth as 215 Hz. However, our equivalent circuit results do not match with these results. In equivalent circuit analysis we find that the fundamental resonance frequency

of the transducer is 1500 Hz and the bandwidth is 750 Hz. The comparison of these results is shown in Table 3.

	Equivalent Circuit Results	**FEM Results**
Fundamental Resonance Frequency	1500 Hz	925 Hz
Bandwidth	750 Hz	215 Hz
Quality Factor	2	4.3

Table 3 Comparison of Equivalent Circuit and FEM Results

In equivalent circuit analysis we apply equal head and tail masses, which makes $\phi = 2$. In this situation the actual head and tail masses become;

$$M_h = m_h + \rho Al/6 \tag{4.3}$$

$$M_t = m_t + \rho Al/6 \tag{4.4}$$

In appendix II, the contribution of the ceramic stack to the actual head and tail masses is illustrated. In barrel-stave transducer the nodal plane, where the displacement in the axial direction is zero, is the center of the ceramic stack and the contribution of the ceramic stack mass to head and tail masses is the one-sixth of its static mass. Therefore, the corrected head and tail mass formulas for the equal head and tail mass situation, which are given in Eq. 4.3 and Eq. 4.4 are correct.

In equivalent circuit analysis, we take the sound speed inside the PZT-4 material as 4000 m/s. The sound speed inside the PZT-4 material varies between 2930 m/s and 4600 m/s. Therefore; the error in the selection of the sound speed may cause the mismatch between the equivalent circuit and the FEM results.

In the model, the transformation of axial motion on either side of staves to the radial motion is represented by α. For curved staved of rectangular cross section with various values of l_s, unsupported stave length, h, average stave thickness, and r, radius of curvature, α was value calculated using the finite element computations and for $h/l_s \leq 0.1$ and $0.2 \leq l_s/r \leq 1$, the approximate formula for α is found as in Eq. 3.23. In addition, the transformation ratio β is also calculated using the finite element results as in Eq. 3.27.

The reason of the mismatch between the equivalent circuit result and FEM results might be the errors in α and β transformation ratios.

We find out some problems stated above in the equivalent circuit model for barrel-stave flextensional transducers. Equivalent circuit of barrel-stave transducer is complicated and has some problems. Therefore, we have proceeded the design phase with FEM analysis. The equivalent circuit model is improved by modifying some of the equivalent circuit elements as discussed in Section 5.3.

Chapter 5

Finite Element Model (FEM) Model of Barrel-Stave Flextensional Transducer

Transducer design consists of two major steps; equivalent circuit analysis and finite element analysis. Equivalent circuit model contains the lumped element representations of transducer's fundamental elements that have the significant influence on its performance. For some transducer types which has relatively less complicated structure, equivalent circuit results well approximates to the actual results, whereas for transducers that have complicated structure, as in the case of barrel-stave flextensional transducer, representing all significant components in equivalent circuit model may be difficult, so the equivalent circuit results may be erroneous and less reliable.

In finite element analysis, depending on the symmetry of the structure, modeling is carried out in 2D or 3D. Complete structure of the transducer is divided into smaller sub pieces called elements. Reducing the element size, which increases the number of elements used in model proportionally, can increase accuracy in the modeling of transducer. Therefore, with the accurate material properties used in the model and smaller element size, it is possible to design transducers whose predicted results agree well with the measured results [4].

Finite element analysis (FEA) may be initiated with the FEM transducer models without water loading to simulate the operation of the transducer in air. Afterwards, the FEM fluid field is added to the model, which has absorbers at an appropriate distance from the transducer. The reflected pressure waves in water structure causes the degradation in the performance of the transducer. Therefore, at the outer side of the fluid 'ρc' matched absorber elements or special elements that apply infinite acoustic continuation are used. The fluid field must be large enough to apply the proper radiation mass loading to transducer [4].

Fluid elements that constitute the finite element acoustic medium describe the pressure field with pressure values at the nodes of the elements; however, mechanical elements are described with displacement values at the nodes [4].

This chapter focuses on the design of barrel-stave transducer using FEM. In section 5.1 the modeling process of transducer in 3D and the verification of the model with the Bayliss's results are described. Design of barrel-stave transducer for various structural dimensions and materials are described in section 5.2. Lastly, in section 5.3 we make corrections on the equivalent circuit using the FEM results.

5.1 Finite Element Modeling of Barrel-Stave Flextensional Transducer in ANSYS

2-dimensional longitudinal section of convex shell type barrel-stave flextensional transducer is illustrated in Figure 10. Transducer's mid-plane inside the shell, the ring type PZT ceramic materials that operate in thickness mode are placed in reverse polarized order. The dark and the light blue sections in the 2D model represent the polarization directions of PZT elements. Shell

elements are located in the left and right side of the model as red and the head sections which also represented by red are located bottom and top of the model. The electrical insulator section between the PZT ceramics and the head elements are illustrated by purple. All of these transducer elements kept together using the center bolt that is located in the transducer mid-plane.

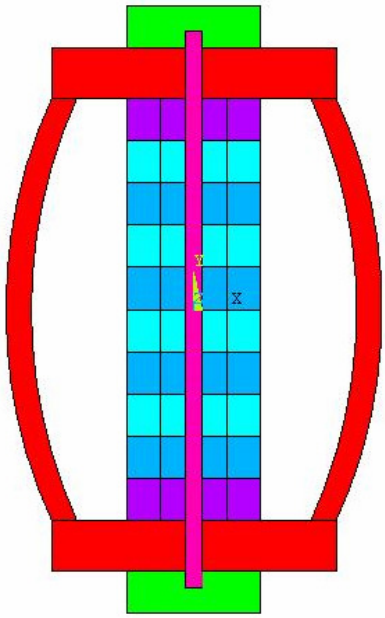

Figure 10 Convex Shell Class-I Flextensional Transducer

2D FEM model cannot be used due to slotted-shell configuration. However, using the symmetry along the half plane of the transducer only the half of the transducer is modeled in 3D. The transducer 3D transducer model in vacuum and in water is illustrated in Figure 11, Figure 12 and Figure 13.

Element types used in the transducer model are given in Appendix III. SOLID5 three-dimensional solid elements are used for PZT, steel, aluminum, macor and araldite elements. For PZT elements UX, UY, UZ and VOLT degree of freedoms (DOF) are chosen, and for other SOLID5 elements UX, UY, UZ DOFs are chosen. SOLID5 has a 3-D magnetic, thermal, electric, piezoelectric

and structural field capability with limited coupling between the fields. The element has eight nodes with up to six degrees of freedom at each node. When used in structural and piezoelectric analyses, SOLID5 has large deflection and stress stiffening capabilities [16]. FLUID30 three-dimensional fluid elements are used to model the acoustical medium. FLUID30 elements that have a contact with solid elements are arranged as the structure present, other fluid elements are set as the structure absent elements. In Figure 14, red elements represent the structure present FLUID30 elements and blue elements represent the structure absent FLUID30 elements. FLUID30 is used for modeling the fluid medium and the interface in fluid/structure interaction problems. Typical applications include sound wave propagation and submerged structure dynamics. The governing equation for acoustics, namely the 3-D wave equation, has been discretized taking into account the coupling of acoustic pressure and structural motion at the interface [16]. In order to prevent the reflection in the model, the FLUID130 infinite acoustic elements are used at the outer side of the model. FLUID130 simulates the absorbing effects of a fluid domain that extends to infinity beyond the boundary of the finite element domain that is made of FLUID30 elements. FLUID130 realizes a second-order absorbing boundary condition so that an outgoing pressure wave reaching the boundary of the model is "absorbed" with minimal reflections back into the fluid domain [16]. In order to apply the electrical load into the model and calculate the electrical input characteristics of the transducer CIRCU94 elements are used as an independent voltage source and resistor. CIRCU94 is a circuit element for use in piezoelectric-circuit analyses. The element has two or three nodes to define the circuit component and one or two degrees of freedom to model the circuit response [16].

Steel, aluminum, macor, araldite material properties used in the model are given in Appendix I. Transducer model is placed along the z-axis such that four of the ceramic rings polarized along +z axis and the other four along the –z axis. Piezoelectric coefficients used for the finite element analysis are given in

Appendix III. Water density is taken as $\rho = 1000\,kg/m^3$, and sonic velocity inside water medium is taken as $v = 1500\,m/s$.

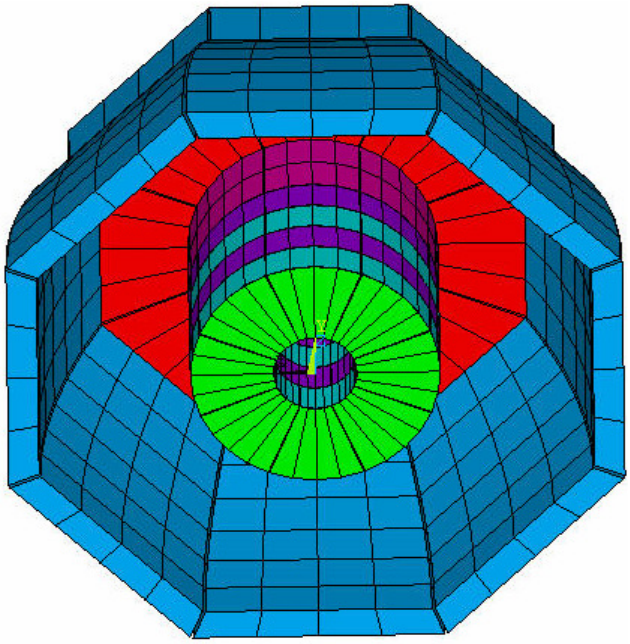

Figure 11 Inside view of the transducer model in ANSYS

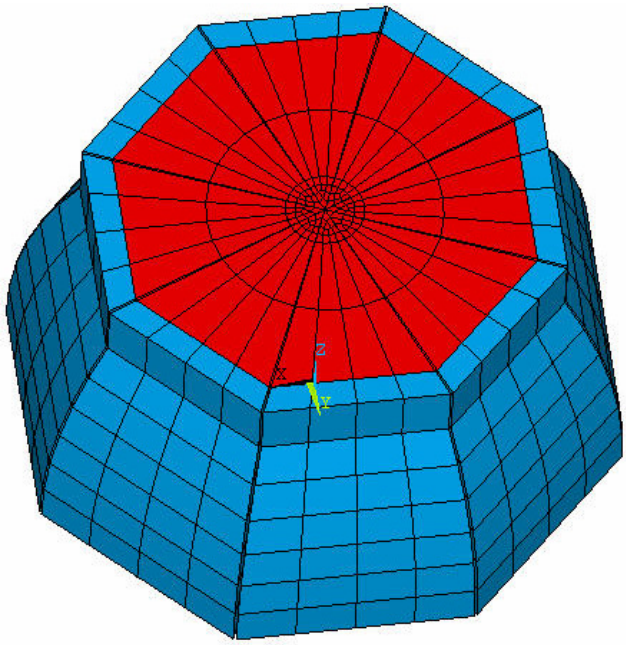

Figure 12 Top view of the transducer model in ANSYS

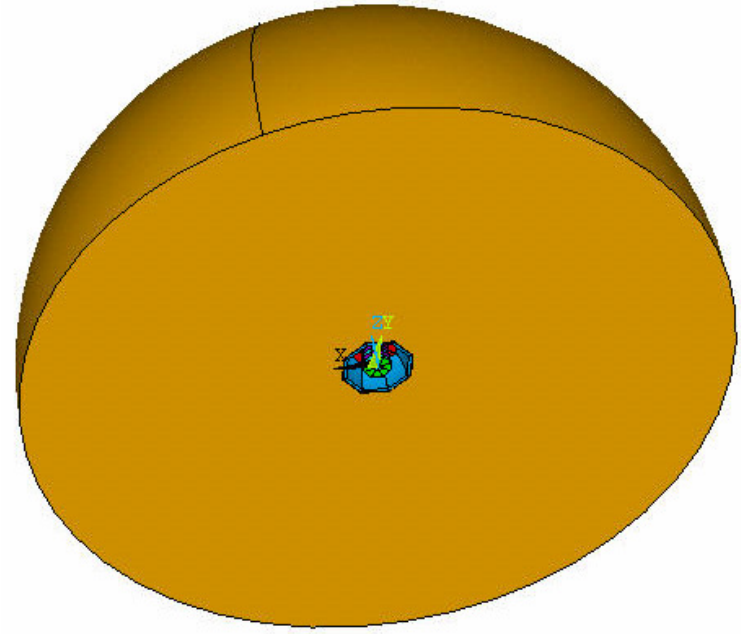

Figure 13 In-water transducer model in ANSYS

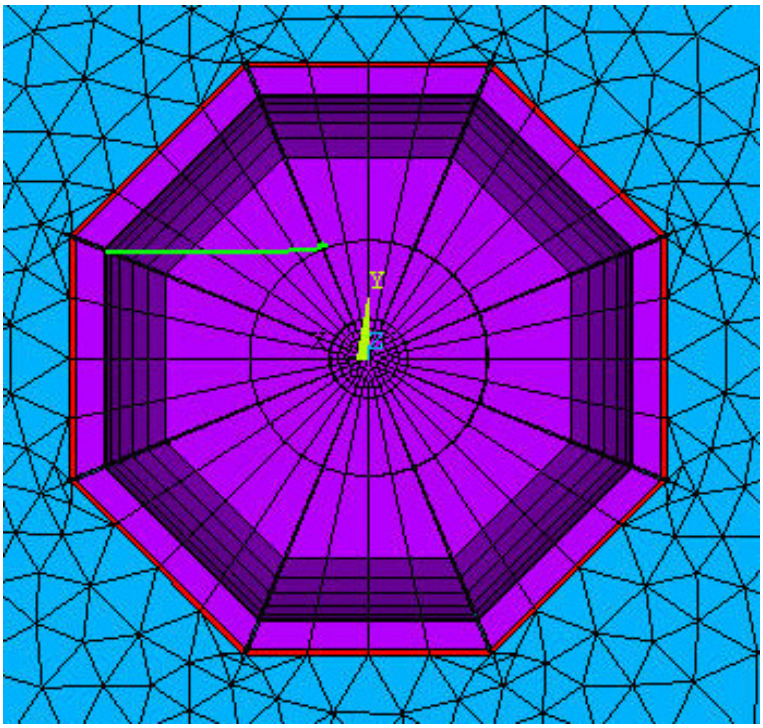

Figure 14 Structure present (red) and structure absent (blue) fluid element types in ANSYS model

Symmetric boundary condition which is the same in our condition as the nodes at z=0 do not move along the z-direction is applied to the model.

We have constructed the structure of the shell slightly different than the Bayliss. He has taken reference point of the radius of curvature and thickness variables of the shell part from the mid-point; however, we take them from the sides of the shell. Therefore, using the same variable set, we get thinner shell, and expect to obtain lower resonance frequency.

Harmonic analysis is performed on the model constructed using the structural dimensions and material properties given in Table 8 and Table 9 in Appendix I, and by a stepped frequency points the conductance and susceptance seen from the input terminals are obtained as in Figure 15 and Figure 16, respectively.

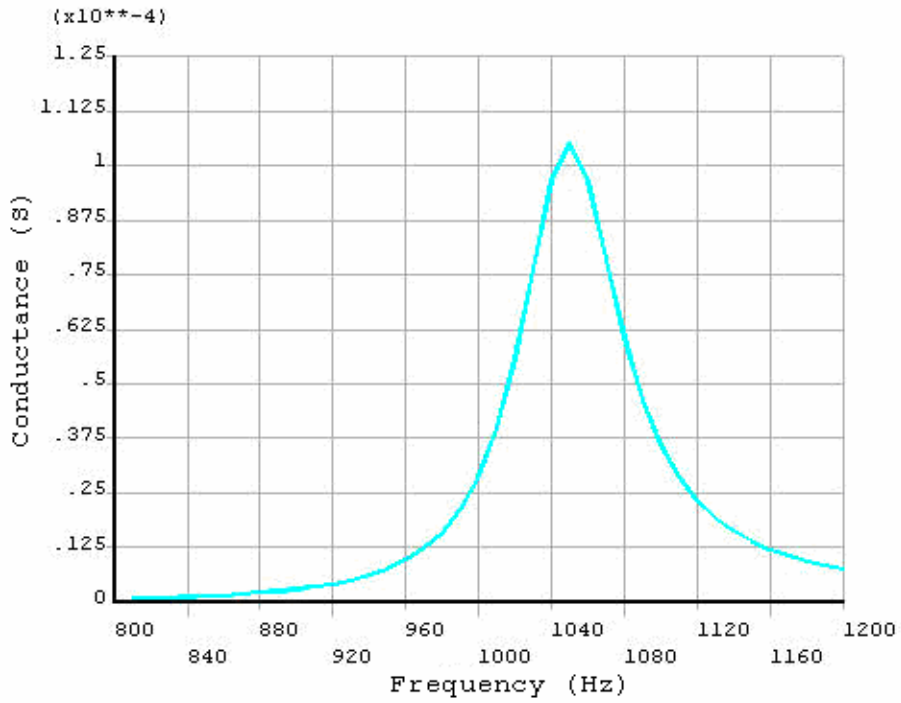

Figure 15 Conductance seen from the input terminals of transducer obtained from FEM

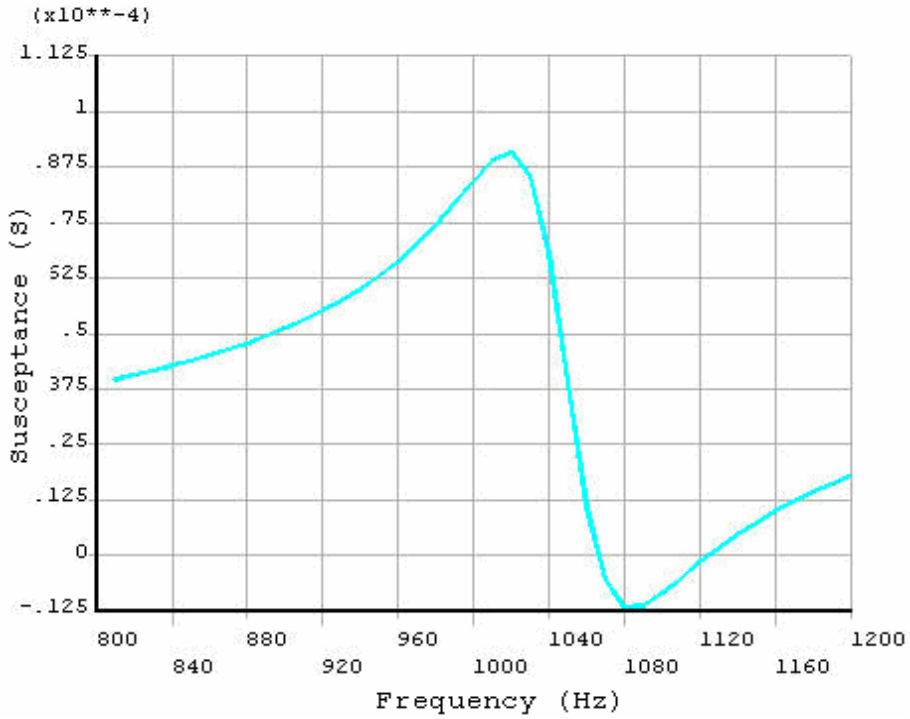

Figure 16 Susceptance seen from the input terminals of transducer obtained from FEM

The resonance frequency and quality factor obtained in FEM analysis is so different than the expected given in Table 3. We realize that the water elements located just at the outer part of the gaps between shells effect the actual behavior of the transducer in a way of increasing the Q-factor and also increase the resonance frequency. Hence, we remove the water elements just over the gaps as shown in Figure 17 and obtain the conductance and susceptance seen from the input terminals as in Figure 18 and Figure 19, respectively.

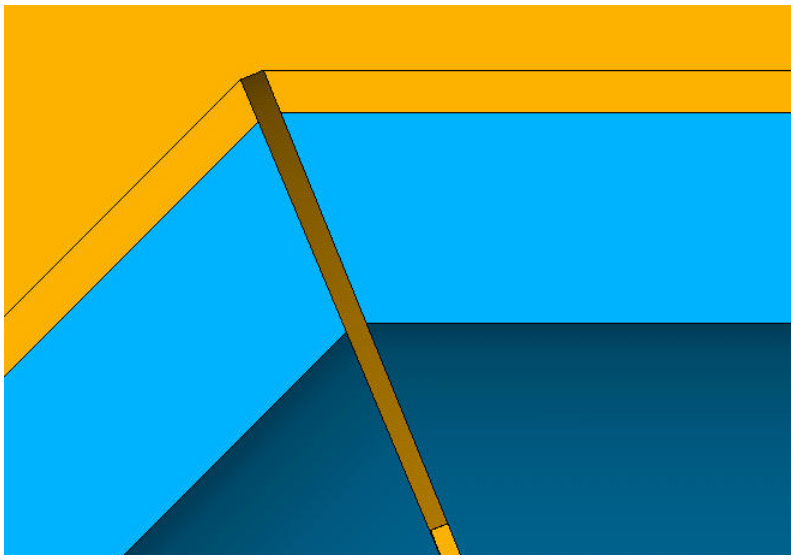

Figure 17 Removed water elements just above the gap between the shell components

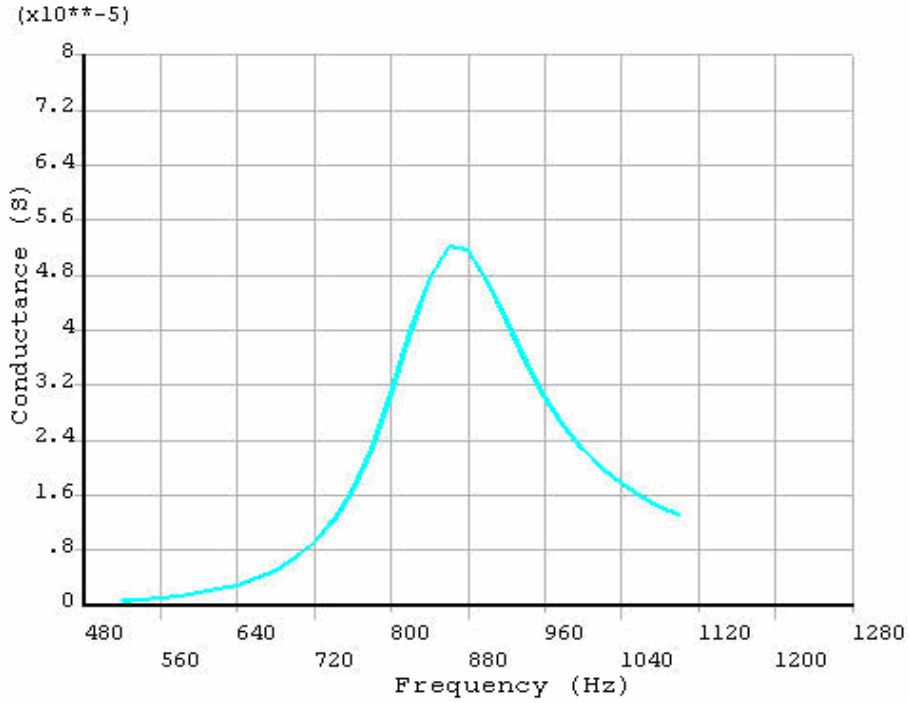

Figure 18 Conductance seen from the input terminals of transducer obtained from FEM

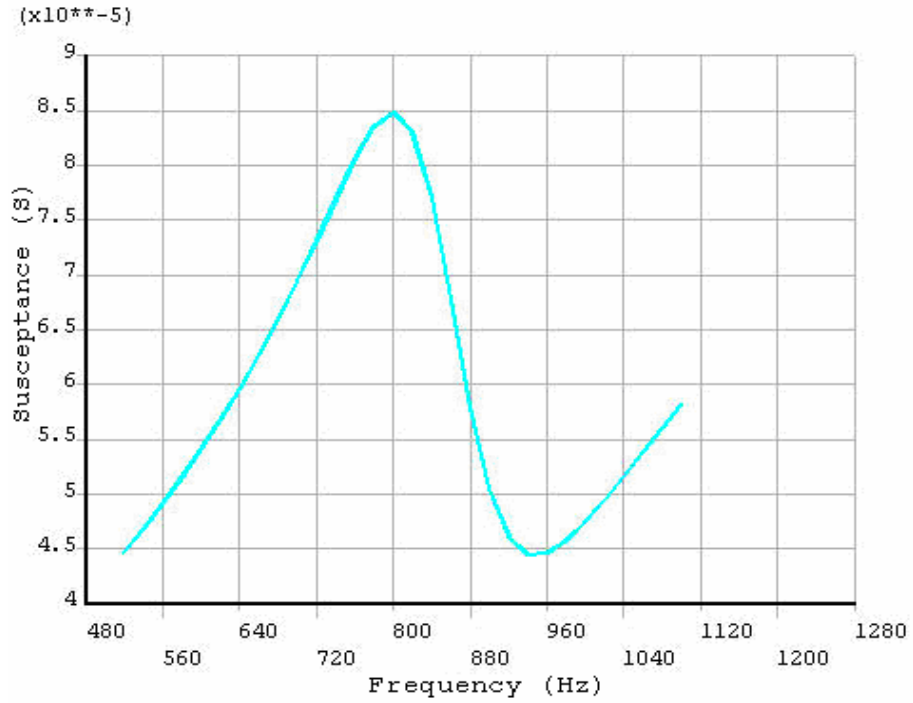

Figure 19 Susceptance seen from the input terminals of transducer obtained from FEM

The fundamental resonance frequency obtained in our FEA is lower than the Bayliss's results as expected; however, the conductance and susceptance values at these frequencies and Q-factors are identical as summarized in Table 4.

	Our FEM Results	**Bayliss's FEM Results**
Fundamental Resonance Frequency	860 Hz	925 Hz
Bandwidth	200 Hz	215 Hz
Quality Factor	4.3	4.3

Table 4 Comparison of our ANSYS results and Bayliss's FEM results

5.2 Barrel-Stave Flextensional Transducer Design in ANSYS

Preliminary design phase should be the equivalent circuit analysis in transducer design. We don't follow the same procedure due to errors we encounter in equivalent circuit as mentioned in chapter 4. Therefore, we design the barrel-stave transducer for low resonance frequency and wide bandwidth in FEM using the PZT4 rings with $r_i = 12.7mm$, $r_o = 38.1mm$, $h = 6.35mm$ shown in Figure 20.

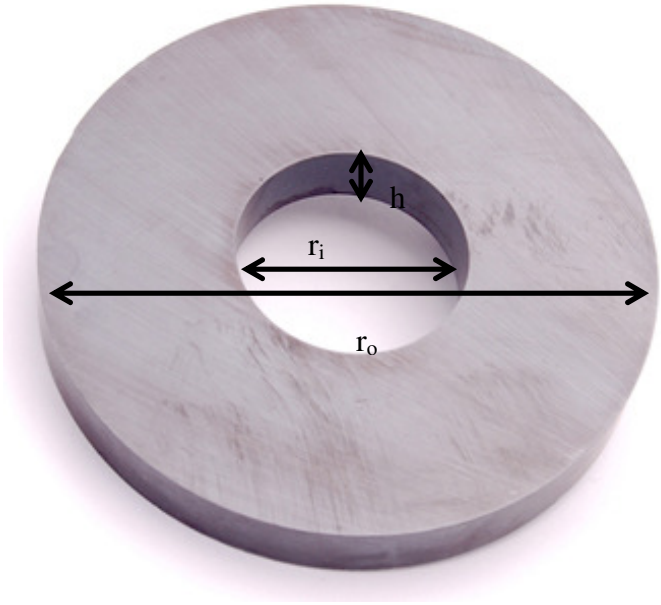

Figure 20 PZT4 rings used in FEM analysis

During the design phase we work on the optimization of eight structural variables for low quality factor that are given in Appendix I. Two of the structural variables belong to PZT ceramic dimensions, which we have chosen before the design phase. For staved-shell barrel-stave flextensional transducers increasing the number of staves has the effect of increasing the resonance frequency and acoustic power of the transducer. Increase in the number of staves

beyond eight has minor effect on the performance of the transducer so we decide to form the shell part from eight number of staves [7]. Therefore, we optimize the Q-factor of the transducer using five structural parameters which are; radius of curvature of shell profile, r, shell thickness, t, length of device between end plates, l, radius at end of device, r_e, thickness of end plate, h_p.

We have completed three different designs changing the five structural parameters and using the materials in Table 9 in Appendix I. For each of the design configurations we obtain the results listed in Table 5.

Design	Parameter	Description	Value
D1	**t**	Radius of curvature of shell profile	0.1m
	t	Shell thickness	5mm
	l	Length of device between end plates	10cm
	r_e	Radius at end of device	50mm
	h_p	Thickness of end plate	10mm
	r_i	Inner radius of the ceramic stack	12.7mm/2
	ro	Outer radius of the ceramic stack	38.1mm/2
	n	Number of staves forming the shell	8
	f	Fundamental Resonance Frequency	1730 Hz
	B	Bandwidth	350 Hz
	Q	Q-factor	4.94
D2	**r**	Radius of curvature of shell profile	0.1m
	t	Shell thickness	10mm
	l	Length of device between end plates	12cm
	r_e	Radius at end of device	50mm
	h_p	Thickness of end plate	10mm
	r_i	Inner radius of the ceramic stack	12.7mm/2
	ro	Outer radius of the ceramic stack	38.1mm/2
	n	Number of staves forming the shell	8

	f	Fundamental Resonance Frequency	2240 Hz
	B	Bandwidth	500 Hz
	Q	Q-factor	4.48
D3	**r**	Radius of curvature of shell profile	0.08m
	t	Shell thickness	5mm
	l	Length of device between end plates	8cm
	$\mathbf{r_e}$	Radius at end of device	40mm
	$\mathbf{h_p}$	Thickness of end plate	10mm
	$\mathbf{r_i}$	Inner radius of the ceramic stack	12.7mm/2
	ro	Outer radius of the ceramic stack	38.1mm/2
	n	Number of staves forming the shell	8
	f	Fundamental Resonance Frequency	2920 Hz
	B	Bandwidth	880 Hz
	Q	Q-factor	3.32

Table 5 Structural design parameter values and in-water performance characteristics of the staved shell transducer

We have changed the shell material from aluminum to carbon/fiber epoxy. Using the material properties for carbon fiber epoxy given in Appendix I we obtain the results listed in Table 6.

Design	Parameter	Description	Value
D4	**r**	Radius of curvature of shelf profile	0.08m
	t	Shell thickness	5mm
	l	Length of device between end plates	8cm
	$\mathbf{r_e}$	Radius at end of device	40mm
	$\mathbf{h_p}$	Thickness of end plate	10mm
	$\mathbf{r_i}$	Inner radius of the ceramic stack	12.7mm/2
	ro	Outer radius of the ceramic stack	38.1mm/2
	n	Number of staves forming the shell	8

	f	Fundamental Resonance Frequency	4950 Hz
	B	Bandwidth	1700 Hz
	Q	Q-factor	2.91

Table 6 Structural design parameter values and in-water performance characteristics of the staved shell transducer for carbon/fiber epoxy shell element

For aluminum shell configuration and D3 structural parameter set given in Table 5, the conductance and susceptance seen from the input terminals are obtained as in Figure 21 and Figure 22, respectively and for carbon/fiber epoxy shell configuration and D4 structural parameter set given in Table 6, the conductance and susceptance seen from the input terminals are obtained as in Figure 23 and Figure 24, respectively.

Shell material properties have significant effect on the acoustical performance of the transducer. The ideal material for low frequency application must have a low stiffness and a high density, whereas for low quality factor applications the ideal material must have a high stiffness and a low density [7]. Carbon/fiber epoxy shell yields low quality factor, and high resonance frequency, whereas aluminum shell yields somewhat higher quality factor, and lower resonance frequency.

Production of carbon/fiber epoxy is more sophisticated, and needs higher quality production process compared to aluminum. Therefore, we choose to produce the aluminum shell design with the structural parameters given in D3 in Table 5.

For aluminum shell configuration and D3 structural parameter set given in Table 5, the vacuum conductance and susceptance seen from the input terminals are obtained as in Figure 25 and Figure 26. SPL of the transducer is given in Figure 27, which corresponds to the maximum power of 232W.

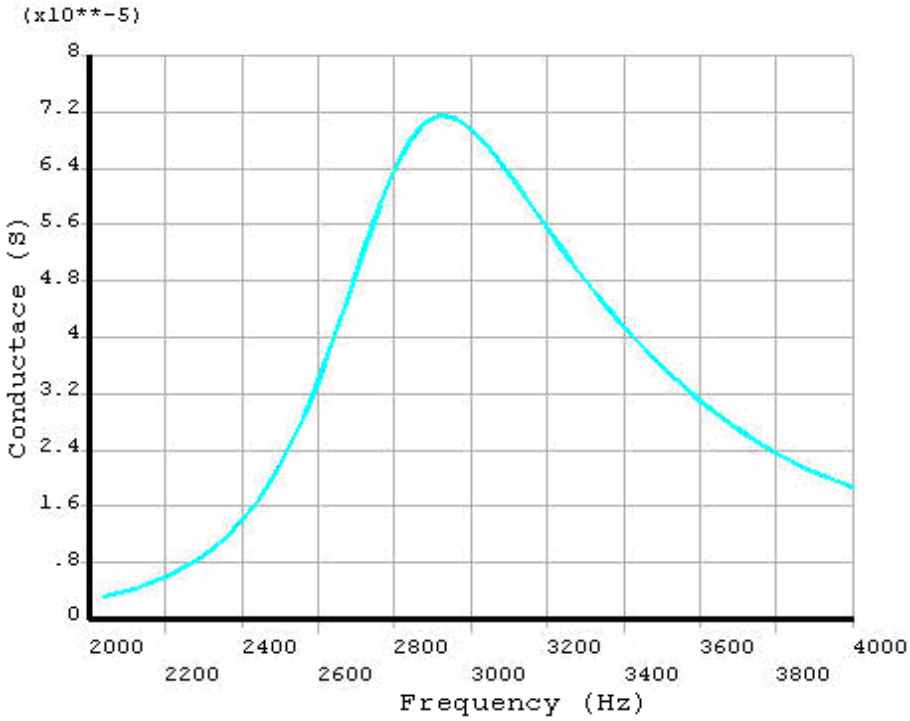

Figure 21 Conductance seen from the input terminals of transducer for aluminum shell and D3 design configuration

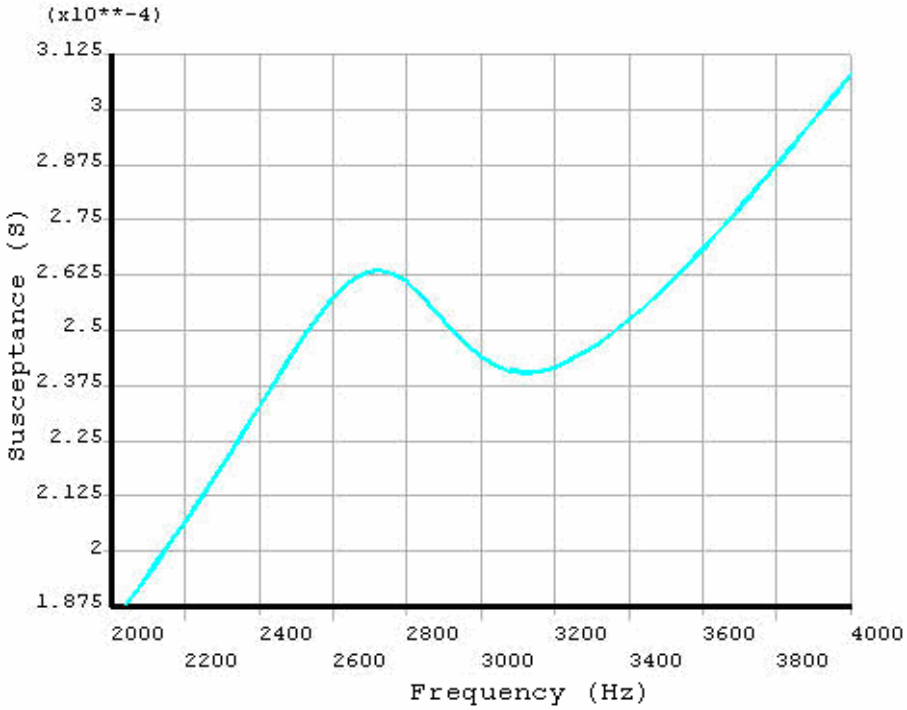

Figure 22 Susceptance seen from the input terminals of transducer for aluminum shell and D3 design configuration

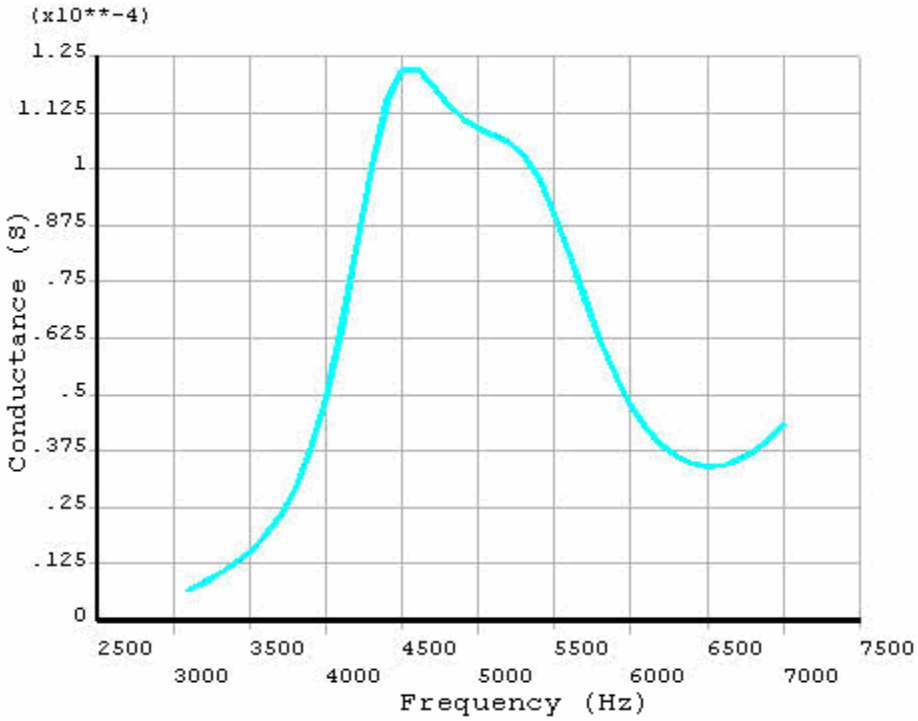

Figure 23 Conductance seen from the input terminals of transducer for carbon/fiber epoxy shell and D3 design configuration

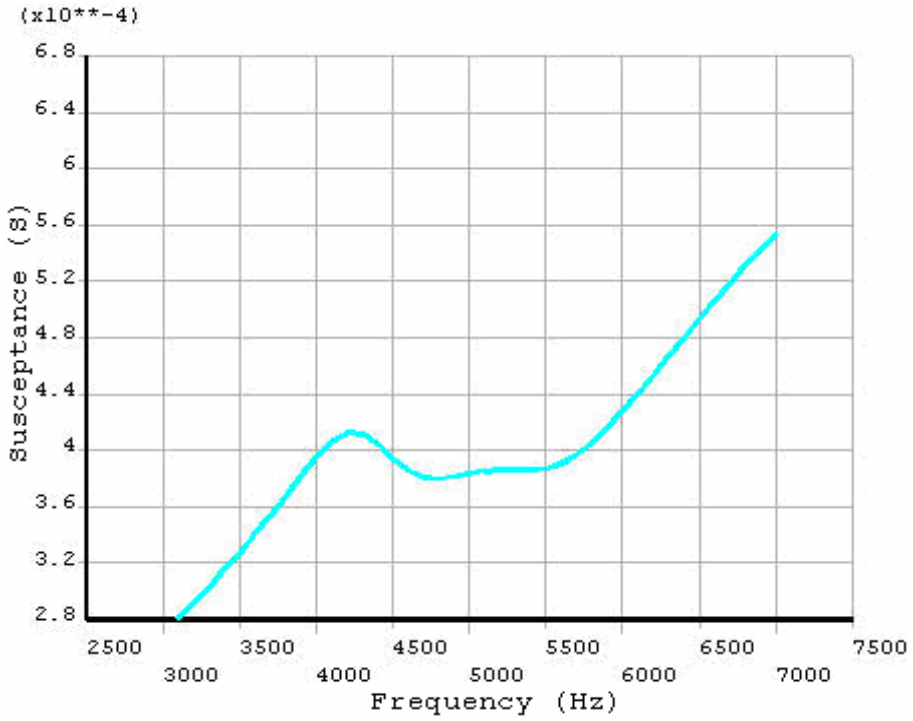

Figure 24 Susceptance seen from the input terminals of transducer for carbon/fiber epoxy shell and D3 design configuration

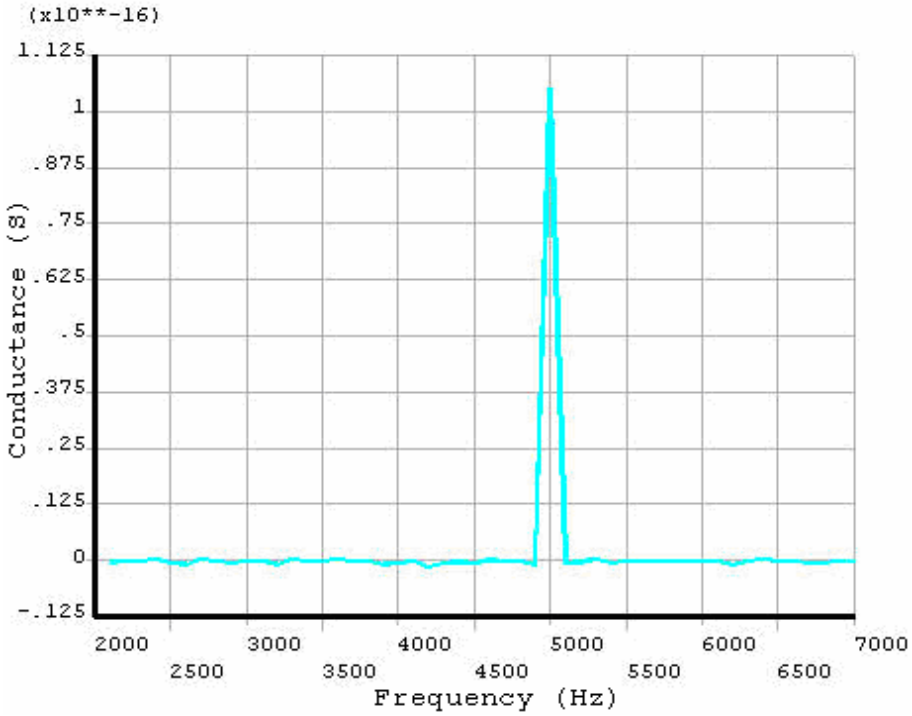

Figure 25 Vacuum Conductance seen from the input terminals of transducer for aluminum shell and D3 design configuration

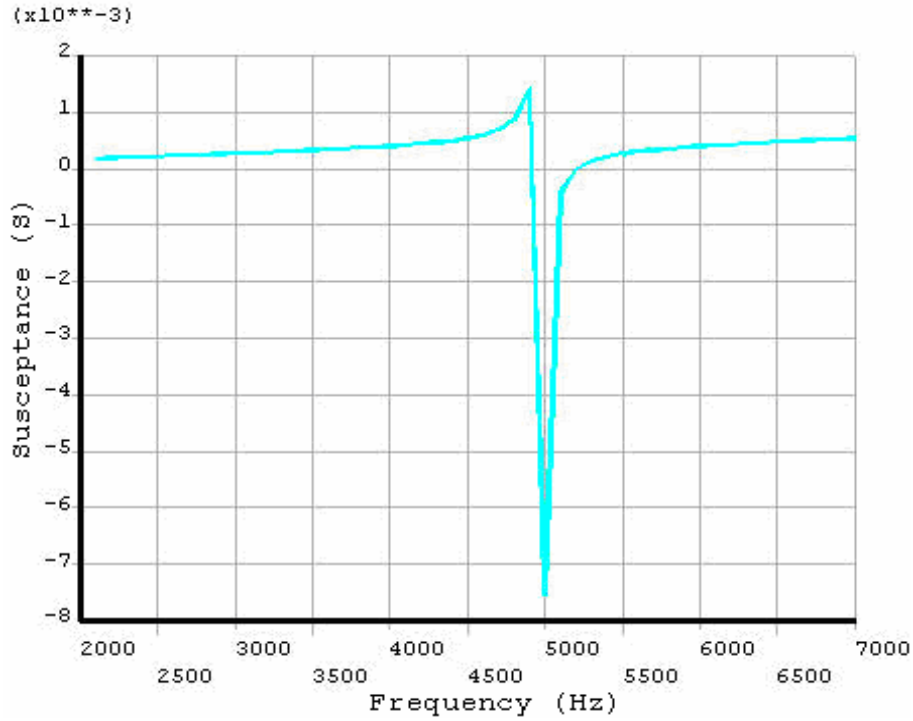

Figure 26 Vacuum Susceptance seen from the input terminals of transducer for aluminum shell and D3 design configuration

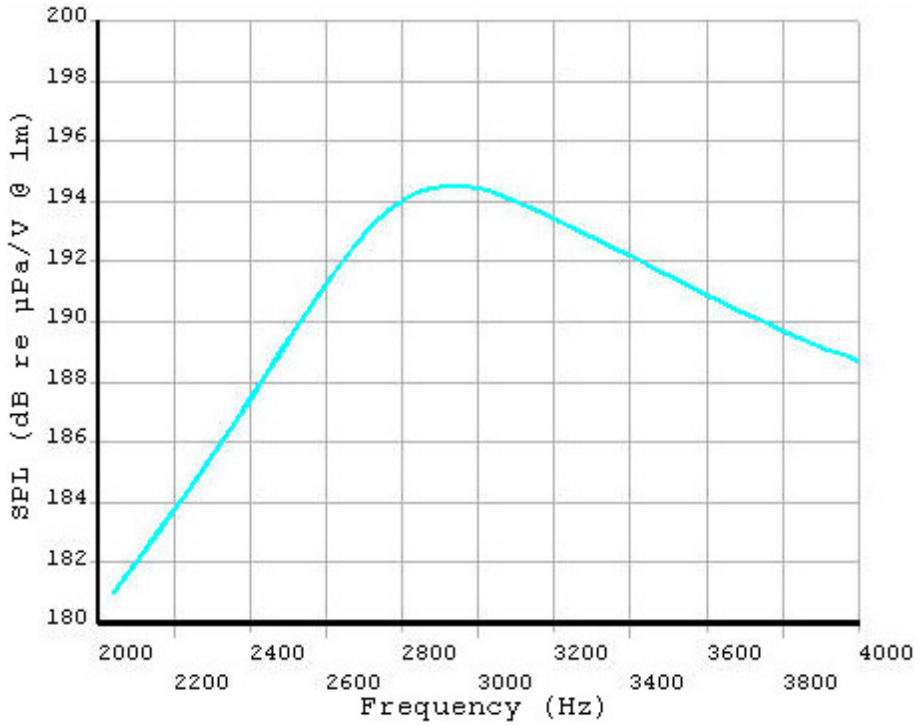

Figure 27 Source pressure level of barrel-stave transducer obtained from FEM analysis

Normalized directivity functions of barrel-stave flextensional transducer at resonance frequency in horizontal and vertical plane are given in Figure 28 and Figure 29, respectively. Pressure values that are obtained at 0.5m distant from the center of transducer are transferred to 1m using spherical spreading rule. Directivity functions are obtained from the normalized source pressure levels vs. direction plots. Directivity functions in both planes demonstrate that the transducer is omnidirectional. This result is expected since the transducer is small compared with the wavelength at resonance frequency.

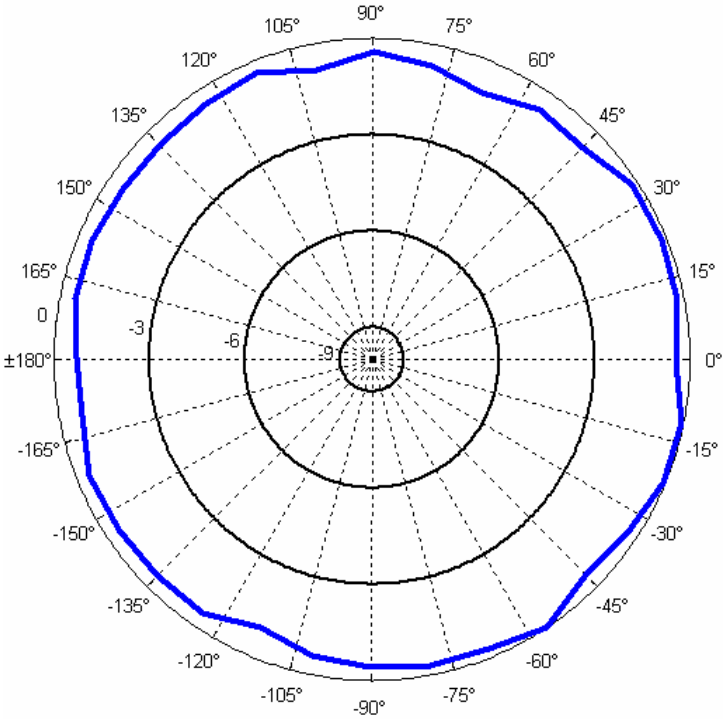

Figure 28 Normalized horizontal directivity pattern of barrel-stave transducer at resonance frequency

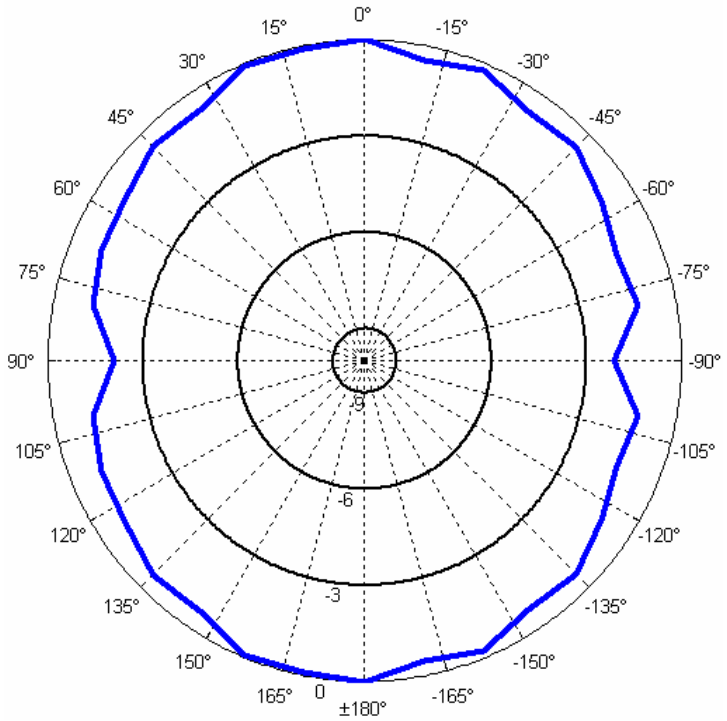

Figure 29 Normalized vertical directivity pattern of barrel-stave transducer at resonance frequency

5.3 Correction on the Equivalent Circuit Using FEM Results

Electrical equivalent circuit model for barrel-stave flextensional transducer requires the knowledge of the sound speed inside the PZT ceramic material to calculate the electromechanical transformation ratio, N, and short circuit compliance of the rings, C_m^E given in Eq. 3.11 and Eq. 3.12, respectively.

Tonpilz type high power and directional transducer's driver side is composed of 33-mode driven ring-stack placed parallel to each other, which is the same as in barrel-stave flextensional transducer type. In mid-frequency applications tonpilz transducers are frequently used and their electrical equivalent circuit is more settled than barrel-stave equivalent circuit model. Therefore, we used the transformation ratio, and ring short circuit compliance formulas used in Tonpilz transducer equivalent circuit model, which is [4];

$$N = nd_{33}A / ls_{33}^E \tag{5.1}$$

$$C_m^E = ls_{33}^E / A \tag{5.2}$$

where s_{33}^E is the elastic compliance coefficient of PZT-4 material.

In the mechanical side of staves, α represents the transformation of axial motion on either side of staves to the radial motion. Using the finite element computations for curved staves of rectangular cross section with various values of h, l_s, and radius of curvature, r, α is approximated as;

$$\alpha \cong 0.83(1 + 0.14 l_s / r) l_s / r \tag{5.3}$$

which is valid for aluminum staves with $h/l_s \le 0.1$ and $0.2 \le l_s/r \le 1$. For our structural dimensions the $h/l_s = 0.0596$ and $l_s/r = 1.0488$, which is outside the approximation set. Therefore, we have calculated α using the FEM results.

α is calculated as;

$$\alpha = \frac{2\xi_{e(average)}}{\xi_{m(rms)}} \tag{5.4}$$

where

ξ_e : *axial displacement*

ξ_m : *radial displacement*

and the rms and average displacements are calculated as in Eq. 3.7 and Eq. 3.8, respectively.

α is calculated using the displacement values on one of eight staves shown in Figure 30. Average axial displacement is calculated from the top 5 nodes' displacement values in z-direction, and rms radial displacement is calculated from the 30 nodes', not including the top 2 row of nodes, displacement values in radially outward direction. Using the average axial displacement and rms radial displacement values calculated using Eq. 3.7 and Eq. 3.8, α values at the frequency range of interest are calculated using Eq. 5.4 and found as in Figure 31.

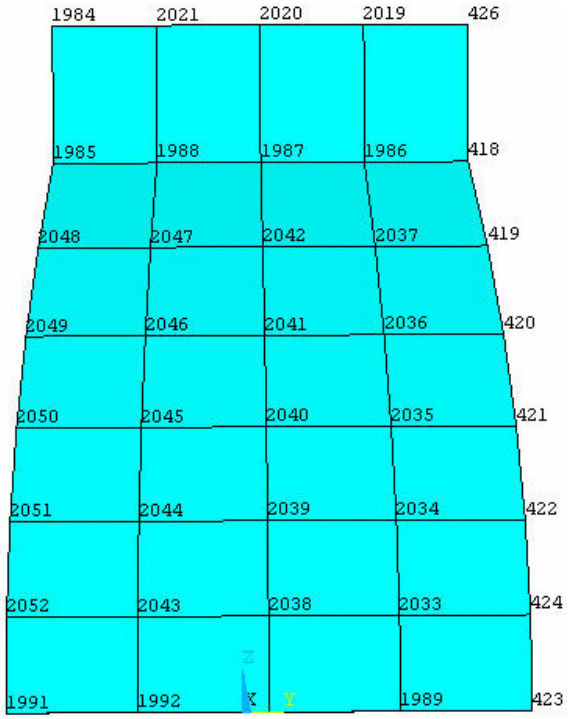

Figure 30 Nodes located on stave that are used to calculate α and β

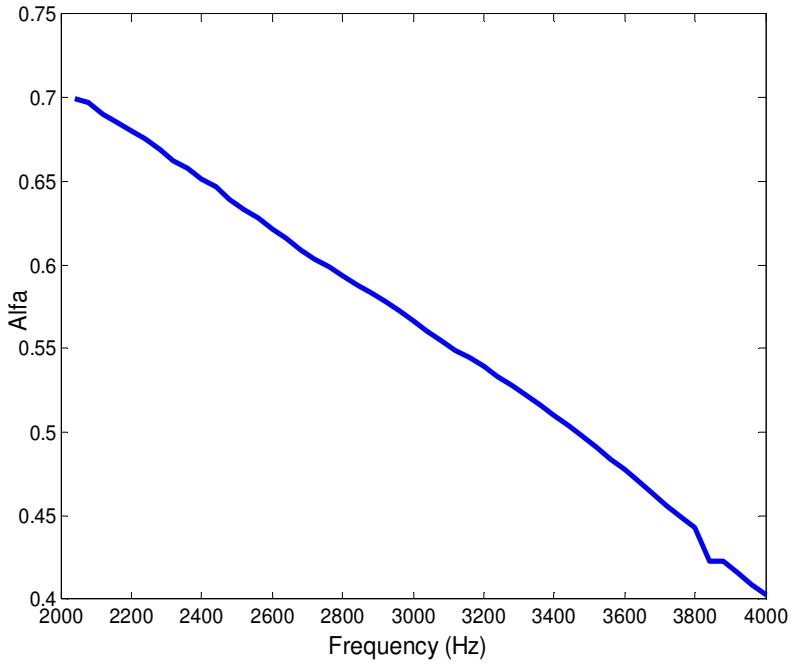

Figure 31 Alfa vs. Frequency obtained using the FEM results

β is the transformation of rms displacement to average displacement on staves in the radial direction and calculated as;

$$\beta = \frac{\xi_{m(rms)}}{\xi_{m(average)}} \tag{5.5}$$

where

ξ_m : *radial displacement*

β is calculated using the displacement values on one of eight staves shown in Figure 30. Radial displacement is calculated from the 30 nodes', not including the top 2 row of nodes, displacement values in x-direction. β values at the frequency range of interest are calculated using Eq. 5.5 and found as in Figure 32.

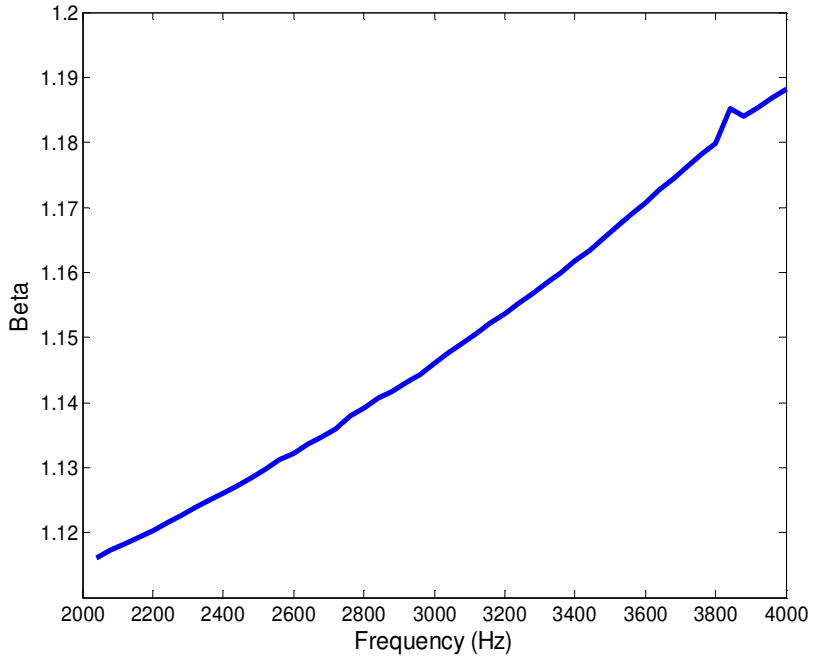

Figure 32 Beta vs. Frequency obtained using the FEM results

The radiation impedance of the barrel-stave transducer used in the model is derived from the radiation impedance of a spherical radiator given as in Eq. 5.6 and in the frequency range of interest the $Z/\rho_0 c_0$ is given in Figure 33 [17].

$$Z_{Sphere} = Area \times \rho_0 c_0 \left[\frac{k^2 r^2}{1+k^2 r^2} + j \frac{kr}{1+k^2 r^2} \right] \tag{5.6}$$

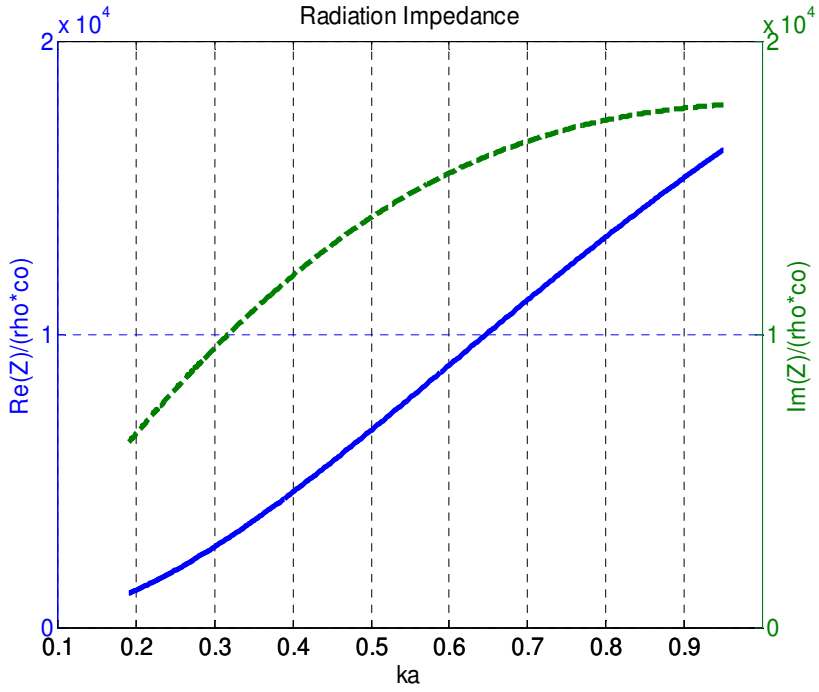

Figure 33 Spherical radiation impedance used in barrel-stave equivalent circuit

Using the obtained α and β values at resonance frequency from the FEM analysis in equivalent circuit model, and putting the transformation ratio and ring short circuit compliance formulas in Eq. 5.1 and Eq. 5.2, the vacuum and in-water conductance-susceptance of electrical equivalent circuit is obtained as in Figure 34 and Figure 35, respectively.

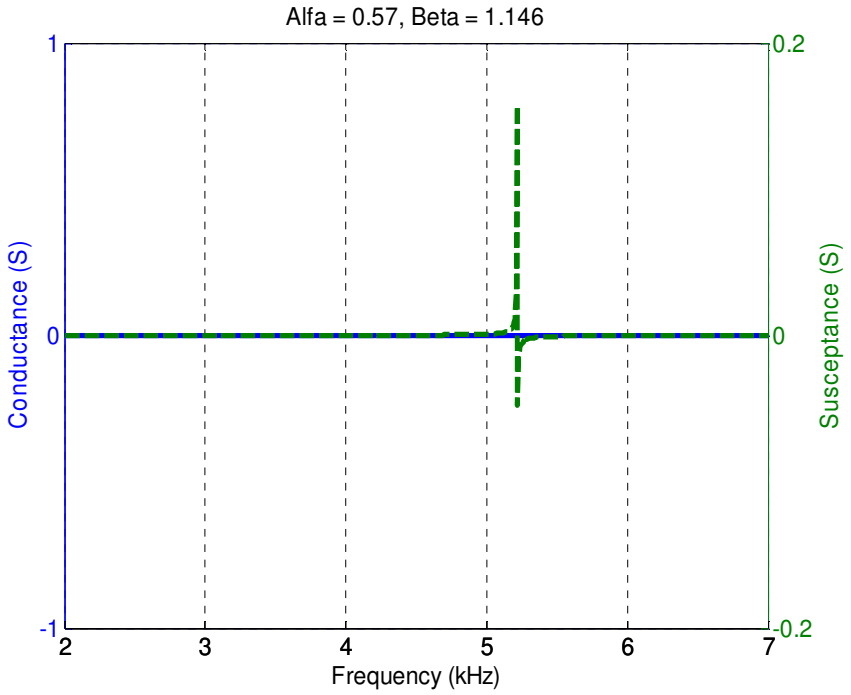

Figure 34 Vacuum conductance-susceptance seen from the electrical terminals obtained from equivalent circuit analysis

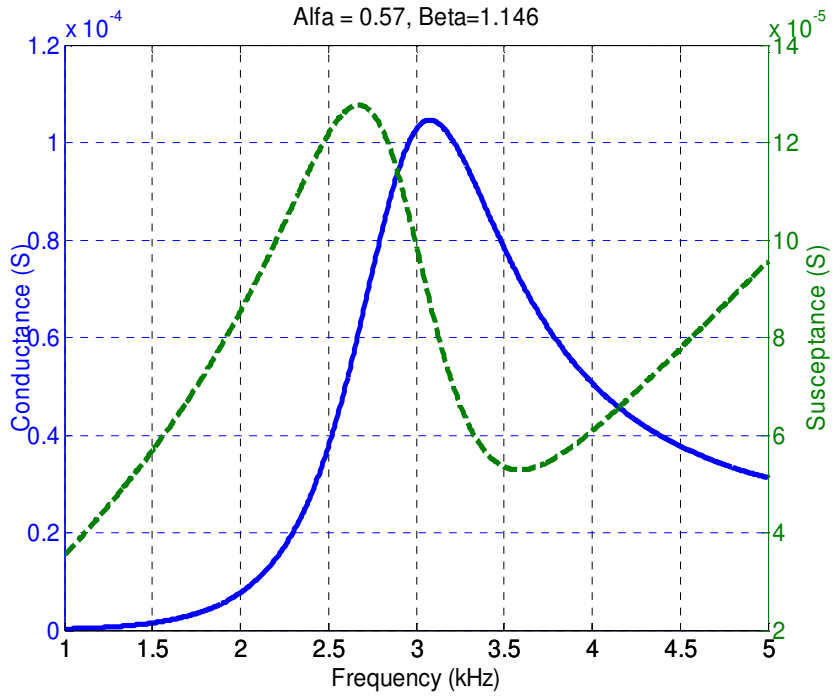

Figure 35 In-water conductance-susceptance seen from the electrical terminals obtained from equivalent circuit analysis

Modifying the electrical circuit results enhances the accuracy of the equivalent circuit; however, there is still a slight difference between the admittance obtained from the FEM and equivalent circuit. The electrical circuit model ignores significant amount of parameters that are considered to have a little effect on the performance of the transducer. However, FEM well approximates the real results so it is more precise. Therefore, the slight difference between the electrical circuit and the FEM results is expected.

Chapter 6

Power Limitations of Barrel-Stave Flextensional Transducer

The maximum power delivered by the transducer is limited by the material limitations used in the design and the acoustical medium characteristics. The material limitations on the maximum power output of the transducer are mainly the maximum electrical field that can be applied to the ceramic materials, the mechanical stress limits of the materials, and the thermal limits.

PZT ceramic materials are polarized in one direction depending on the usage. This polarization vanishes and the depolarization occurs due to electric field, or due to temperature rise. For lead zirconate titonate ceramics Stansfield suggest a limiting electric field of 200 kV r.m.s. m^{-1} [3].

In this chapter, we discuss the effect of cavitation and the thermal characteristics of the transducer on the maximum power output of the transducer.

6.1 Cavitation Limitation for Barrel-Stave Flextensional Transducer

The acoustic power intensity of the sound wave is defined as;

$$I = \frac{p_0^2}{2\rho c} \tag{6.1}$$

As the acoustic power intensity increases, the acoustic pressure increases and in some point it reaches the hydrostatic pressure of the water. If the intensity is increased still further, the acoustic pressure peaks will exceed the hydrostatic pressure of water, and absolute pressure becomes negative at the negative cycle of the acoustic pressure, so cavitation occurs. When the water medium begins to cavitate, the bubbles occur in front of the transducer at the negative cycle of the acoustic pressure cycle [3].

Cavitation causes many undesirable effects on the acoustical performance of the transducer. Firstly, creation of the bubbles causes additional power dissipation, and hence reduces the electro-acoustic efficiency. Secondly, bubbles reduce the acoustical radiating from the transducer. And thirdly, bubbles disturb the linearity of the medium and causes non-linearity in the radiated acoustic pressure wave [3].

Formation of bubbles is a nucleation process and it takes some time. As the frequency of the pressure wave increases, period of negative pressure decreases so the cavitation threshold increases. Also, decreasing the pulse length can increase the cavitation threshold.

As the depth increases, the ambient pressure also increases, and the cavitation threshold increases. Urick defines the cavitation threshold at depth h as [2];

$$I_c = 0.3\gamma\left(P_c(0) + \frac{h}{10} \right)^2 \tag{6.2}$$

For circular piston, plane and hemispherical type transducers γ is in the range of 0.3 and 0.6. In our calculations, we take the worst case, which is $\gamma = 0.3$. Therefore, the cavitation threshold becomes as;

$$I_c = 0.09\left(P_c(0) + \frac{h}{10} \right)^2 \tag{6.3}$$

where h is the depth in meters, $P_c(0)$ is the cavitation threshold pressure at the surface.

For low frequency acoustic signals, the cavitation threshold pressure becomes 1 and increases with frequency as illustrated in Figure 36. Therefore, for f = 3 kHz, the cavitation threshold becomes;

$$I_c = 0.09\left(1 + \frac{h}{10} \right)^2 \tag{6.4}$$

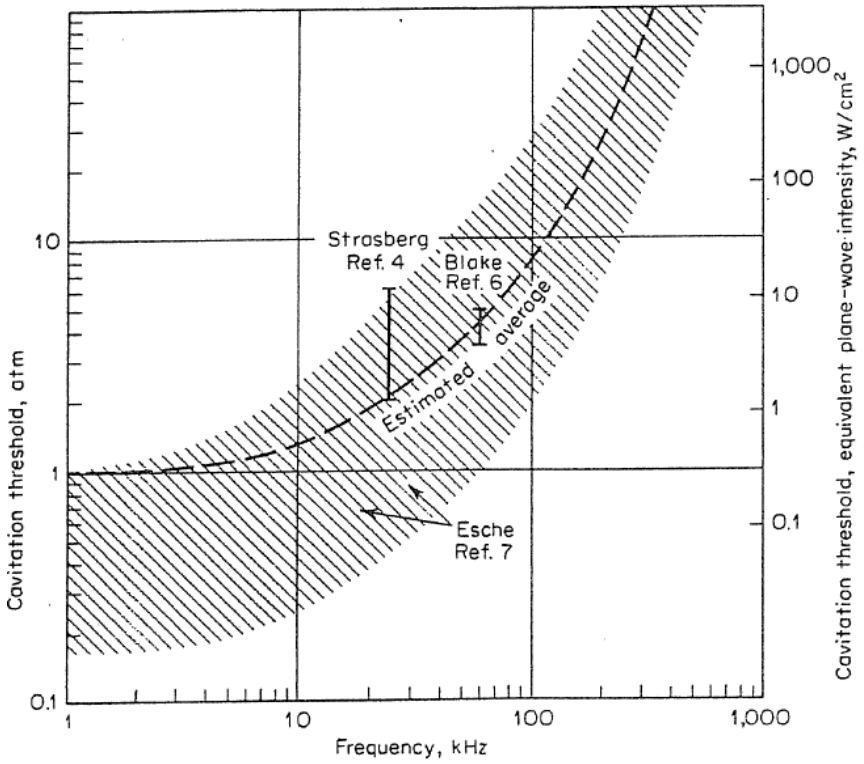

Figure 36 Frequency dependence of cavitation threshold [2]

The maximum continuous wave acoustic power, P_c, that a transducer can radiate at the onset of cavitation is given by;

$$P_c = I_c(h)A \tag{6.5}$$

where A is the radiating surface area of transducer.

Radiating surface area of barrel-stave transducer is 143 cm^2. Therefore, the maximum acoustic wave acoustic power at the onset of cavitation, P_c, with respect to depth is calculated as in Figure 37. Delivery of the maximum power output of the barrel-stave transducer, which is 232 W requires depths more than 33m.

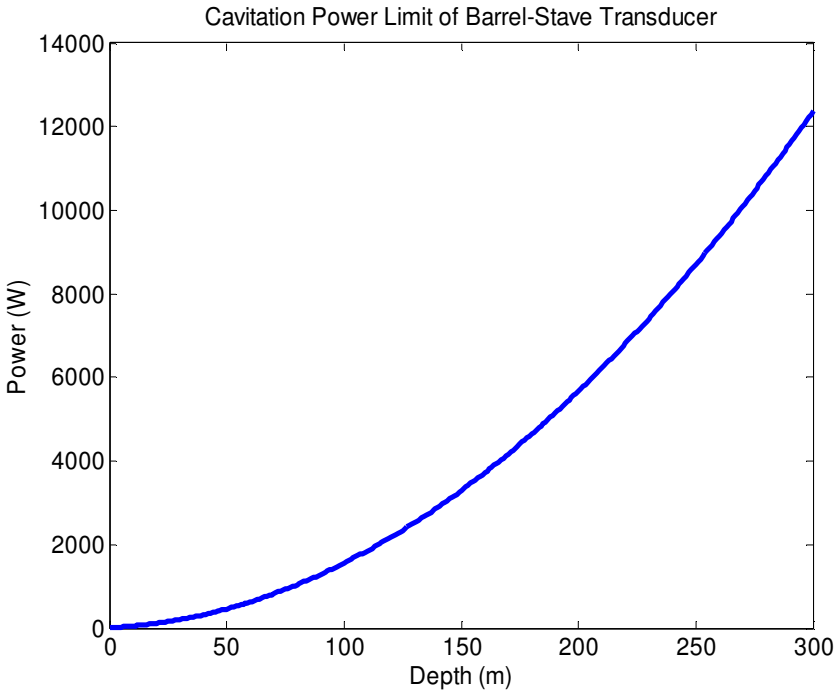

Figure 37 Maximum continuous wave acoustic power of barrel-stave transducer at the onset of cavitation

6.2 Thermal Analysis of Barrel-Stave Flextensional Transducer

The dielectric and mechanical losses result in the generation of heat inside the ceramic material. This heat energy causes the rise in the temperature of the transducer. After a certain temperature limit, called a curie point, PZT materials loose their piezoelectric properties. The Curie temperature for PZT-4 ceramics is 328 °C [18]. Temperature rise is encountered the most in high duty-cycle or continuous wave (CW) operations [7]. In practical applications PZT ceramic temperature aimed to keep well below the Curie temperature, like the half of the Curie temperature point.

In this section, we determine the behavior of the barrel-stave transducer at the electrical limiting voltage of continuous 1796 V_p in vacuum and water

with coating and without coating materials. In addition, we examine the thickness of the coating material on the thermal performance of the transducer.

Thermal analysis of barrel-stave transducer is performed using Flux2D FEM program with the thermal material properties given in Appendix IV. The FEM model formed in Flux2D program is shown in Figure 38.

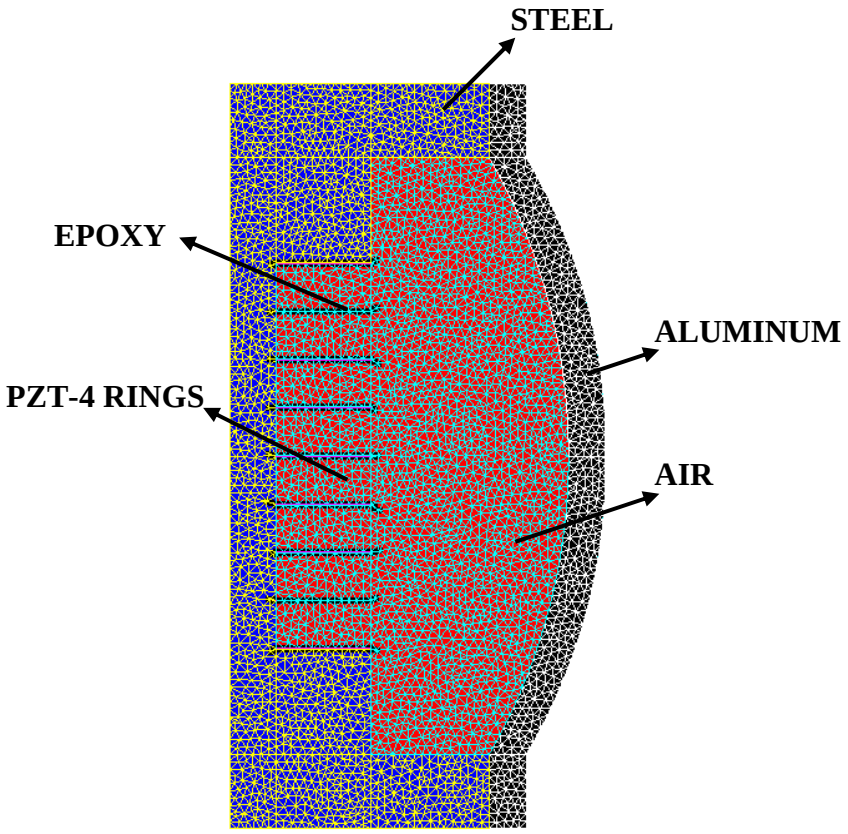

Figure 38 FEM model of Barrel-Stave transducer in Flux2D

Power loss inside the PZT materials is given by Şahin as [19];

$$P_d = wE^2V\varepsilon \tan\delta \tag{6.6}$$

where w is the angular frequency of driven electrical signal, E is the electrical field created inside the PZT rings by the input voltage, V is the total PZT volume, ε is the dielectric constant of PZT rings, and $\tan\delta$ is the loss factor.

In order to take the worst case into consideration, we take the frequency as the upper band frequency that is 3500 Hz, and the electric field as 2000 V/cm. Dependence of the loss factor and the electric field given in Figure 39 [18], and we take the loss factor as 0.02.

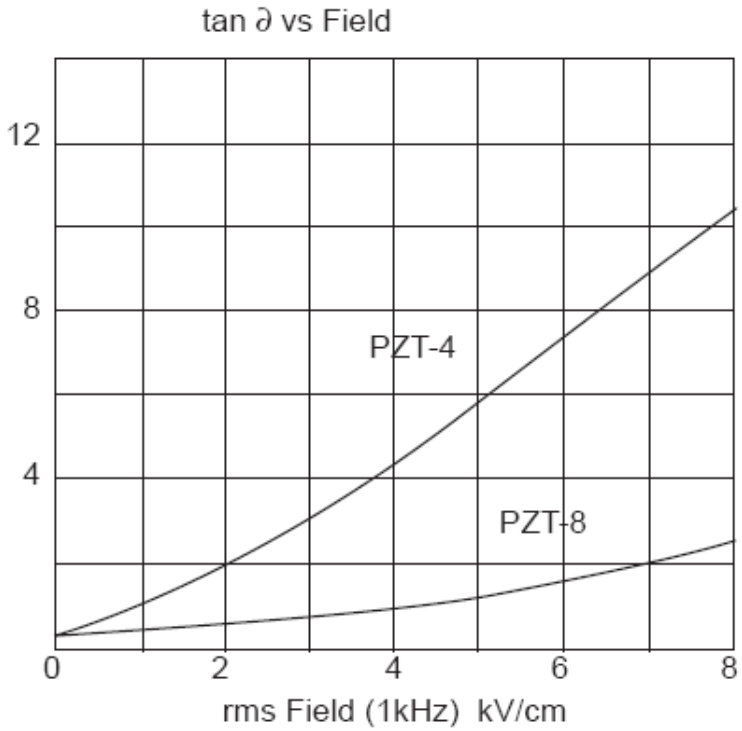

Figure 39 Loss factor vs. rms electric field [18]

In-air steady state and transient temperature response of the barrel-stave transducer are given in Figure 40 and 41, respectively. Transducer temperature reaches steady state at 12000 second and the maximum temperature measured at the center of the transducer is 131 °C.

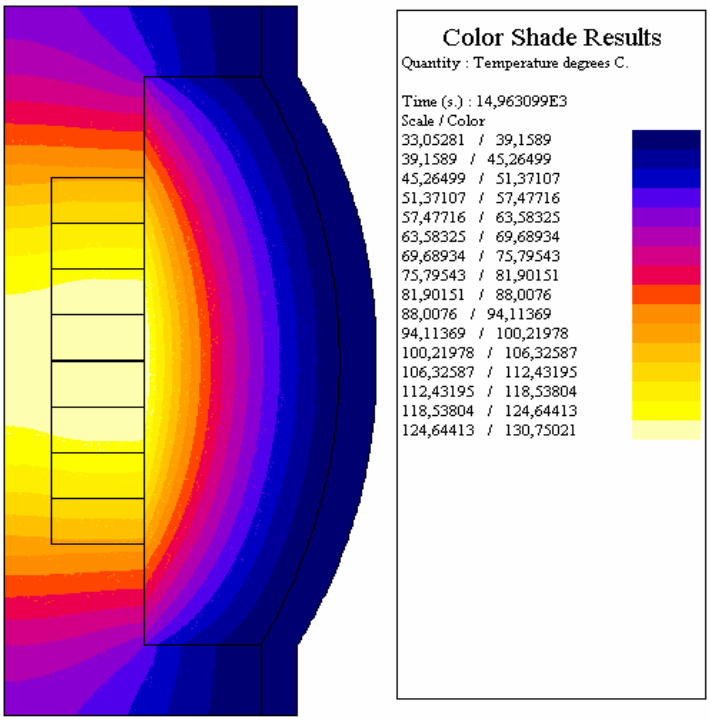

Figure 40 Steady state temperature distribution of barrel-stave transducer in air

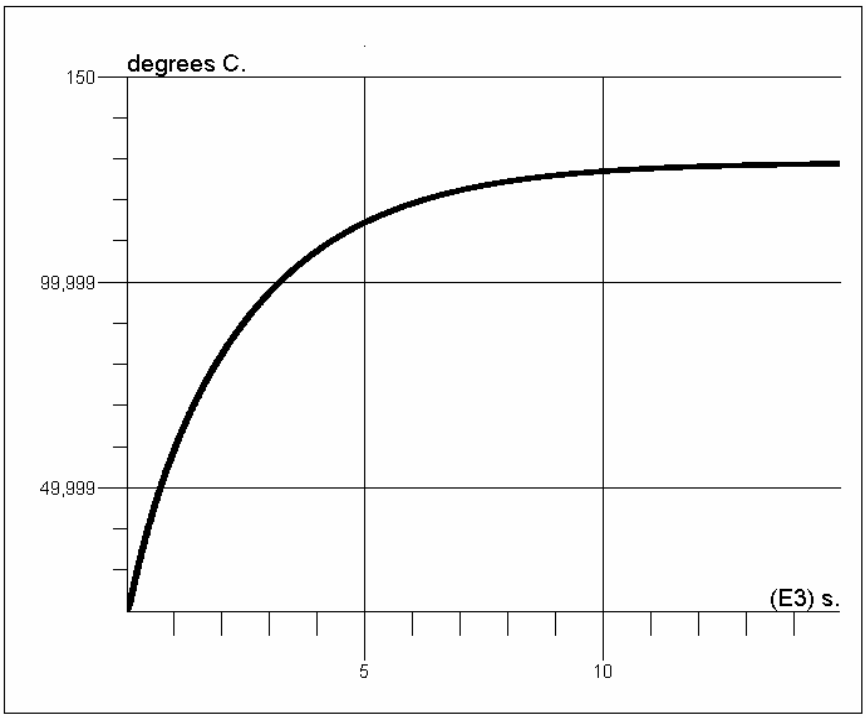

Figure 41 Transient temperature response of barrel-stave transducer taken from the mid point of the model

The convection coefficient of water is approximately the 80 times larger than air, so we expect to obtain lower steady state temperature in water. Steady state and transient temperature response of the barrel-stave transducer in water are given in Figure 42 and 43, respectively. Transducer temperature reaches steady state at 10000 second and the maximum temperature measured at the center of the transducer is 62 °C.

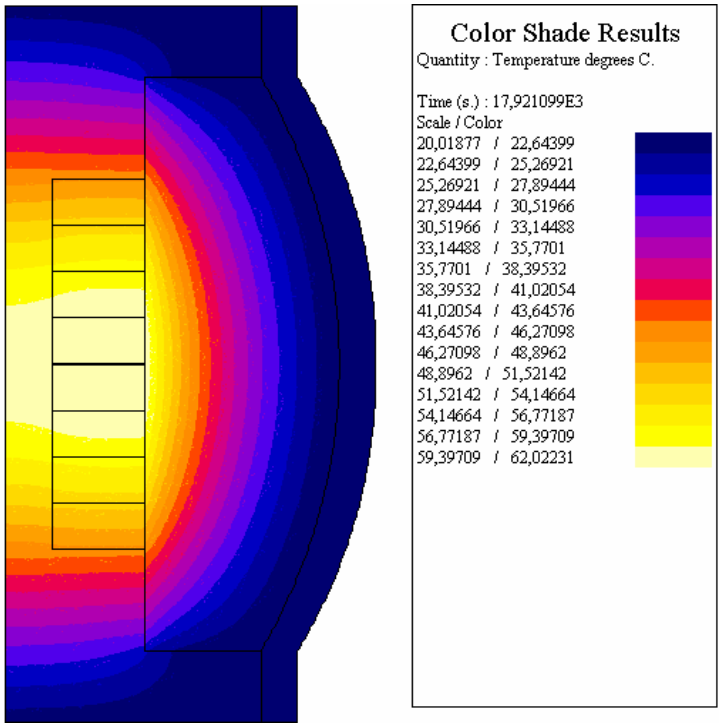

Figure 42 Steady state temperature distribution of barrel-stave transducer in water

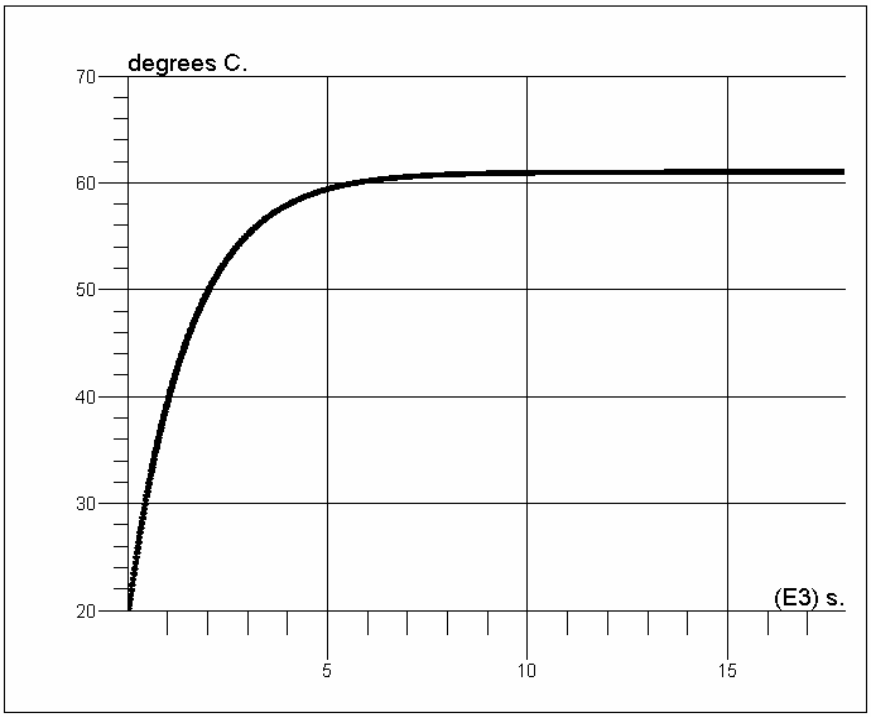

Figure 43 Transient temperature response of barrel-stave transducer in water taken from the mid point of the model

For preventing the water ingression from the gaps between the staves, barrel-stave transducer must be coated with a material. This material affects the temperature response of the transducer depending on its thickness and thermal conductivity properties. We have carried out our analysis with the polyurethane coating material having a thermal conductivity 0.2 W/m°K for 3 mm and 5 mm thickness values.

Steady state and transient results obtained for 3 mm coating is given in Figure 44 and Figure 45, and for 5 mm coating Figure 46 and Figure 47, respectively. For 3 mm coating, we obtain a maximum 68 °C steady state temperature, and for 5 mm coating, we obtain a maximum 70 °C steady state temperature. This temperature levels are well below the Curie point, therefore we conclude that the temperature is not a power limiting factor for our barrel-stave transducer.

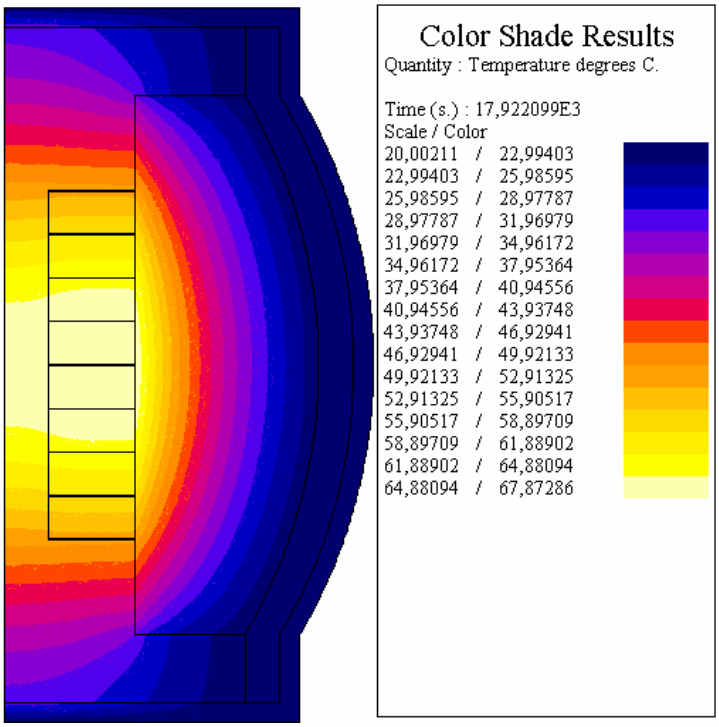

Figure 44 Steady state temperature distribution of barrel-stave transducer in water with 3 mm polyurethane coating

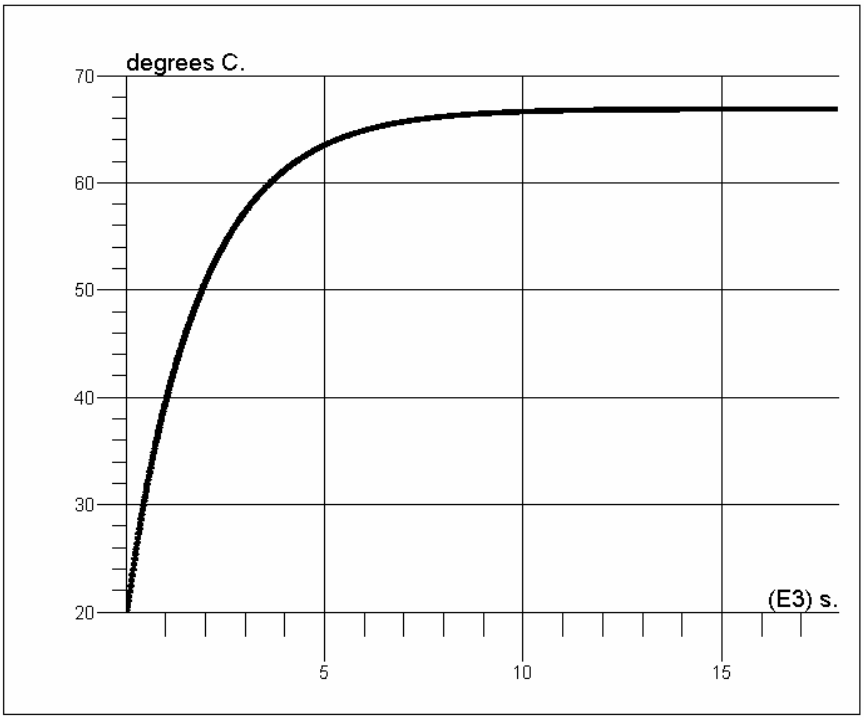

Figure 45 Transient temperature response of barrel-stave transducer in water with 3 mm polyurethane coating taken from the mid point of the model

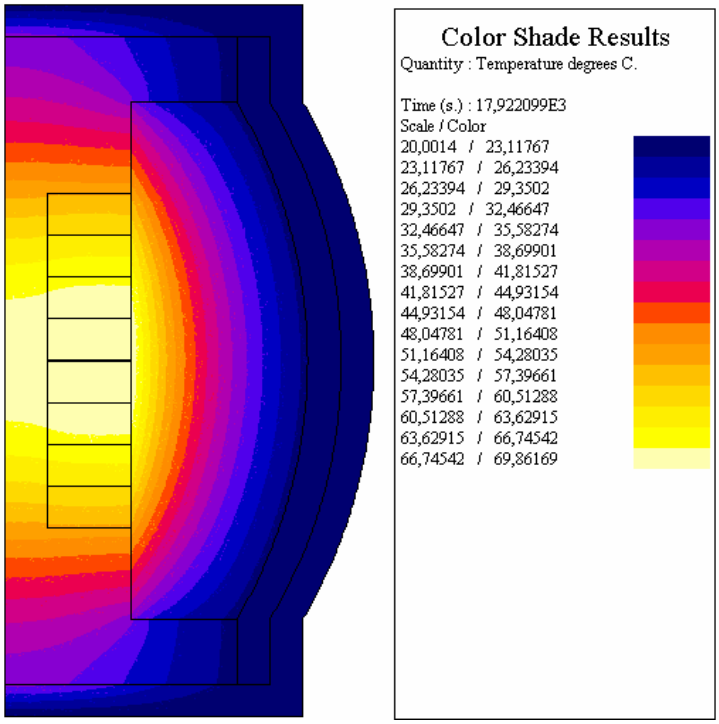

Figure 46 Steady state temperature distribution of barrel-stave transducer in water with 5 mm polyurethane coating

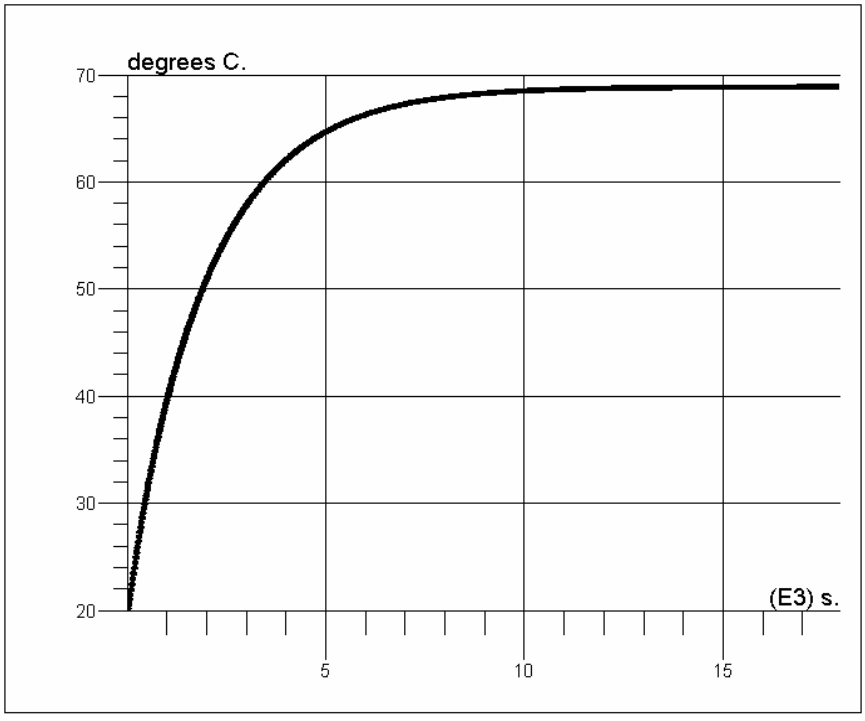

Figure 47 Transient temperature response of barrel-stave transducer in water with 3 mm polyurethane coating taken from the mid point of the model

Chapter 7

Experimental Work

In previous chapters we have discussed the design methods and parameters of barrel-stave flextensional transducer. Using those parameters we have found a design set which has a low quality factor and frequency. This chapter deals with the construction and measurement of designed transducer.

In section 7.1 the construction details of transducer are illustrated. The measured results and comparison of measured results with the theoretical results are described in section 7.2.

7.1 Construction Details of Barrel-Stave Flextensional Transducer

The detailed mechanical drawings of transducer structural elements are given in Appendix V.

The construction of transducer is conducted in three main steps for controlling the construction and results. After each main step we have compared the measured and theoretical results.

We have used the 0.7mm %96 alumina instead of MACOR, which has higher stiffness, higher density and better electrical insulation properties. The

material properties of alumina are illustrated in Appendix I and the dielectric strength of alumina is 9 kV/mm. We have used stainless steel between the alumina and end-plates to maintain the designed length of barrel-stave transducer. The cross-section view of transducer is illustrated in Figure 48.

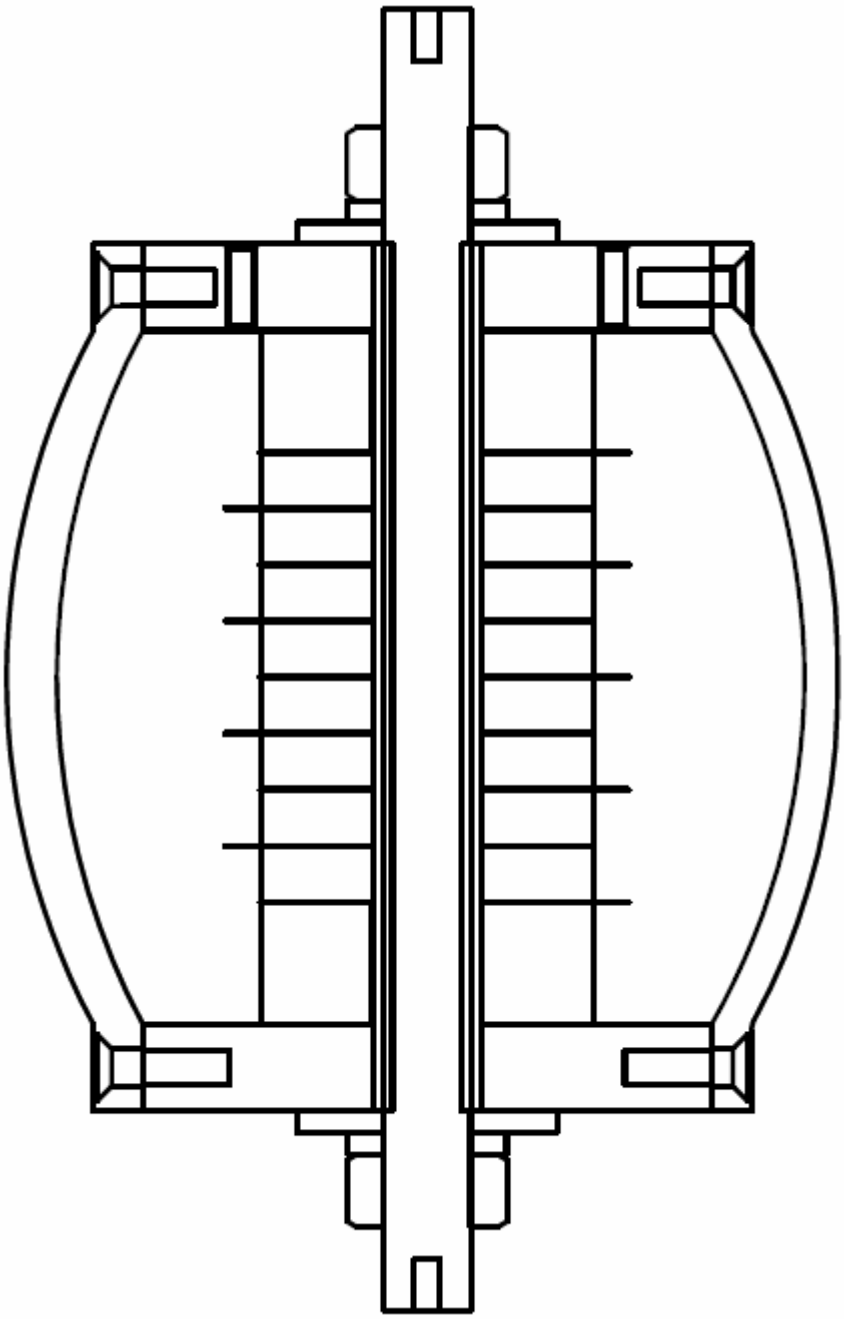

Figure 48 Cross-sectional view of barrel-stave transducer

Before we have glued the components, we have constructed the transducer applying the vaseline between each of the components and test the transducer in air. Measurements are taken for the transducer without the aluminum staves and with the aluminum staves, and compared these results with the theoretical results as shown in Appendix VI.

Afterwards, we have constructed the ceramic stack with end-plates and glue them. The photograph of the constructed assembly is depicted in Figure 49.

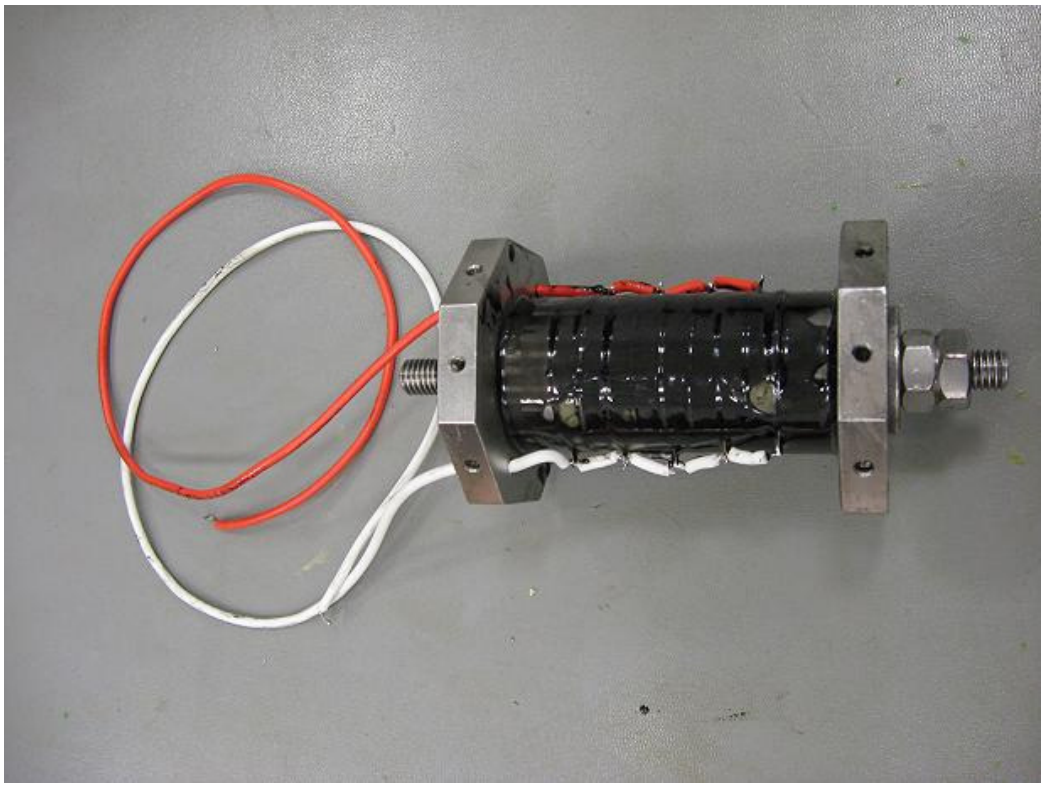

Figure 49 Barrel-stave transducer without aluminum staves

After construction we have applied pre-stress on the ceramic stack. For the most difficult operating condition of 150 m depth and 1796 V applied voltage we have obtained the maximum displacement, $\Delta\ell$, on ceramic material as 1.57 μm and corresponding strain, S, value to this displacement is calculated as;

$$S = \Delta\ell / \ell = 1.574\mu m / 6.35mm \cong 2.5\times10^{-4} \tag{7.1}$$

where ℓ is the thickness of one PZT-4 ceramic ring.

After that, we have calculated the stress value using the calculated strain and young's modulus of PZT-4 ceramic as;

$$T = E\times S = 193\times10^{9}\times2.5\times10^{-4} = 48.25MPa \tag{7.2}$$

Total charge generated on ceramic ring is calculated using the piezoelectric constant, d_{33}, ring electroded area, A, and the stress obtained in Eq. 7.2 as;

$$Q = d_{33}TA = 289\times10^{-12}\times48.25\times10^{6}\times10^{-3} \cong 14\mu C \tag{7.3}$$

Using this charge, the voltage created on the ceramic ring is calculated as;

$$V = \frac{Q}{C} = \frac{14\mu C}{0.9nF} = 15.56kV \tag{7.4}$$

where C is the input capacitance of the ceramic ring.

We have measured the voltage on the ceramic rings using $10M\Omega$ voltmeter, and used additional capacitor of $6\mu F$ in parallel to ceramic rings. Therefore, the voltage drops to $V = 2.53V$, and the RC time constant increases to 1 minute, which is enough to pre-stress and read the voltage on the voltmeter.

In second step we glued the aluminum stave to the constructed structure in step 1. The photograph of the transducer assembly with staves is depicted in Figure 50.

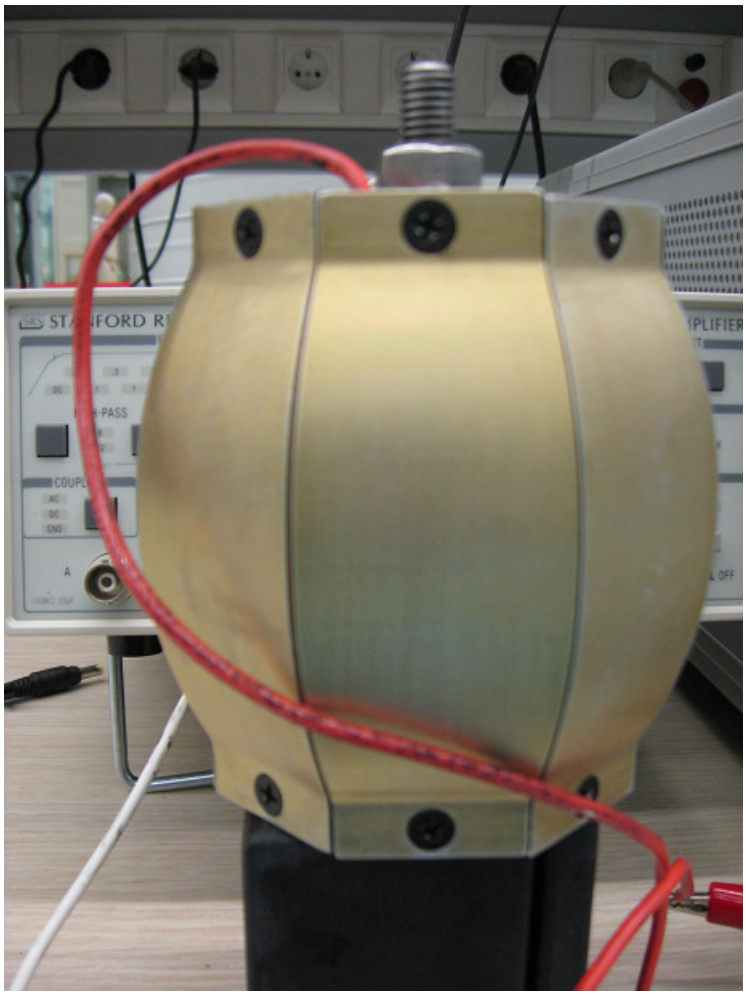

Figure 50 Barrel-stave transducer with aluminum staves

Lastly, we have sealed the transducer using the silicon material. The photograph of the final transducer assembly is depicted in Figure 51.

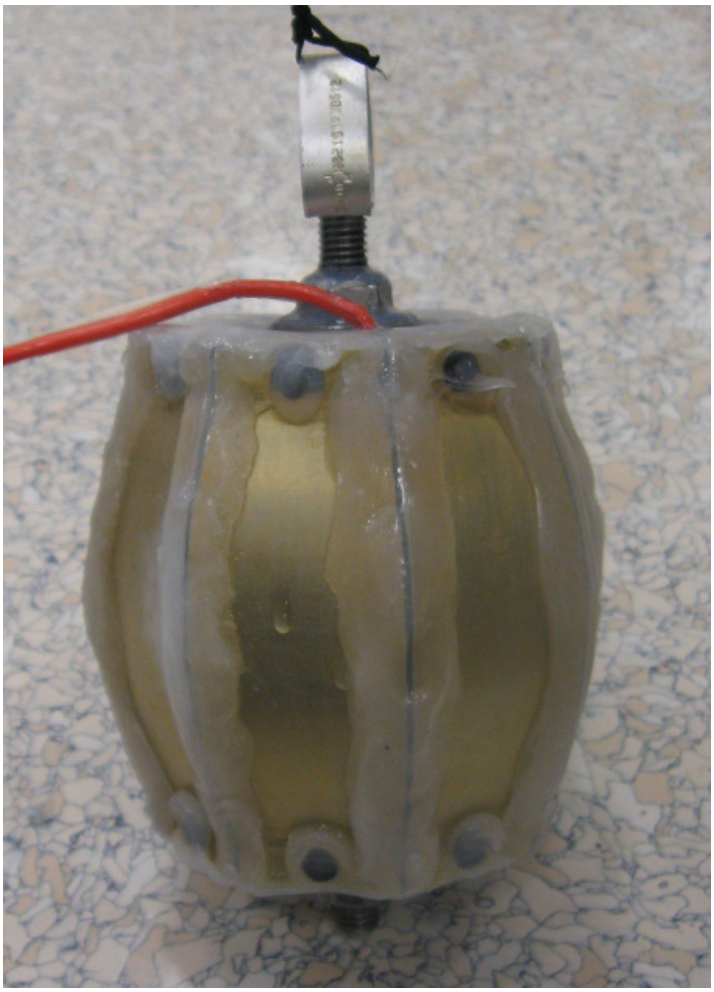

Figure 51 Barrel-stave transducer sealed with silicon

7.2 Measured Results of Barrel-Stave Flextensional Transducer

The in-air measured admittance of transducer without aluminum staves is obtained as in Figure 52. We obtain the 10.65 kHz measured resonance frequency which is well approximates to the resonance frequency obtained in numerical result which is 10.7 kHz.

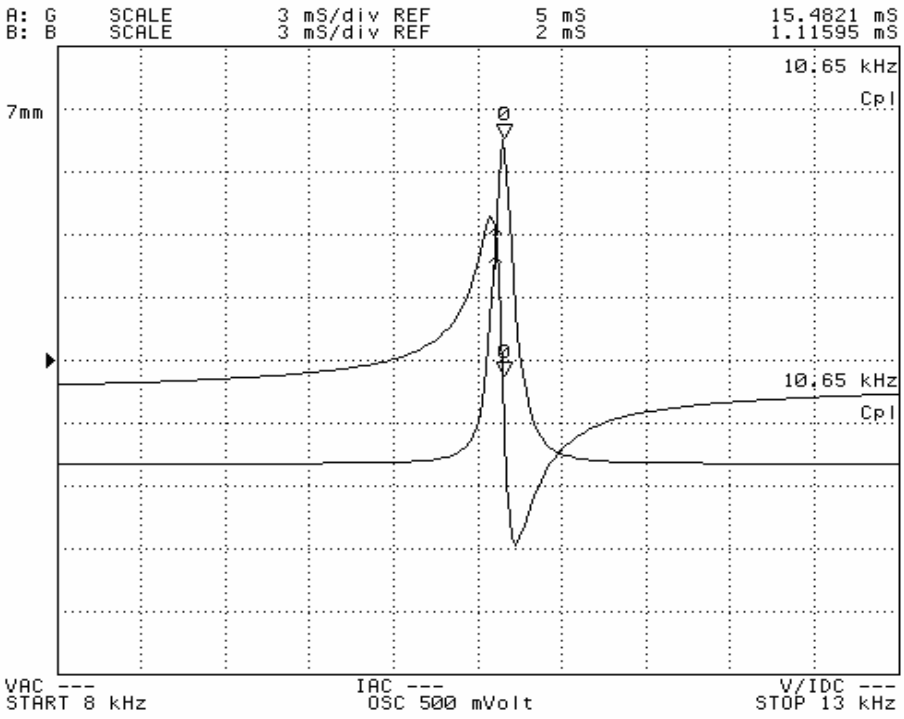

Figure 52 Measured in-air input admittance of transducer without aluminum staves

The in-air measured admittance of transducer with aluminum staves is obtained as in Figure 53. We obtain the 4.73 kHz measured resonance frequency which is well approximates to the resonance frequency obtained in numerical result which is 5 kHz.

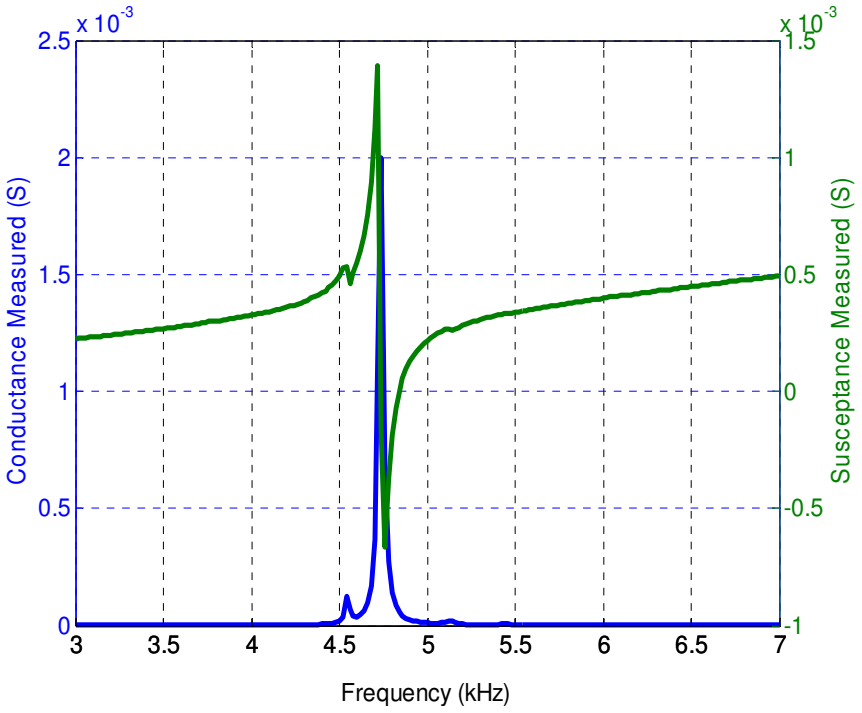

Figure 53 Measured in-air input admittance of transducer with aluminum staves

Admittance measurement is conducted in 2m x 2m and 1.5m deep water tank locating in ASELSAN as shown in Figure 54. We have used burst signal type rather than continuous to decrease the effects of reflections. Measurements are taken using the program written in Agilent VEE. Measurements are tried to be conducted in the steady state region of transducer. Transducer reaches its steady state depending on its quality factor. Barrel-stave transducer's quality factor is 3.32 that mean transducer needs approximately 3.5 wavelengths to reach steady state. At frequency of 1.5 kHz this corresponds to 3.5m, and at frequency of 3 kHz this corresponds to 1.75m. Our measurement tank is not big enough to get the data in steady state region before the reflections reach the transducer. Therefore, we expect to get erroneous data from the water tank measurements.

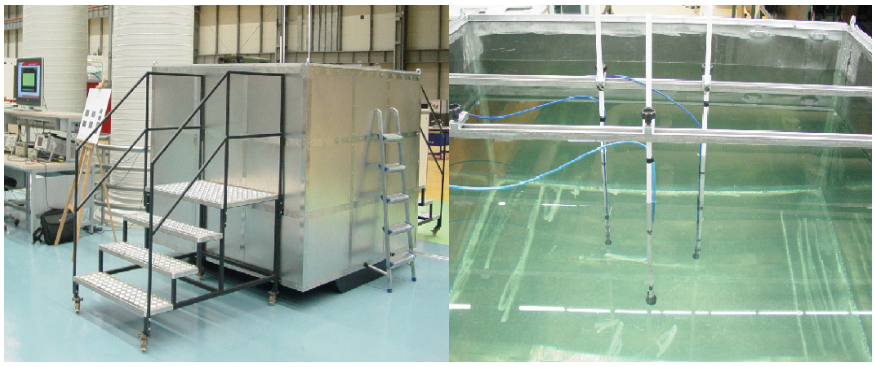

Figure 54 Water tank with dimensions 2mX2m and 1.5m deep.

Figure 55 and Figure 56 illustrates the comparison of ANSYS and measured in-water conductance and susceptance of transducer, respectively.

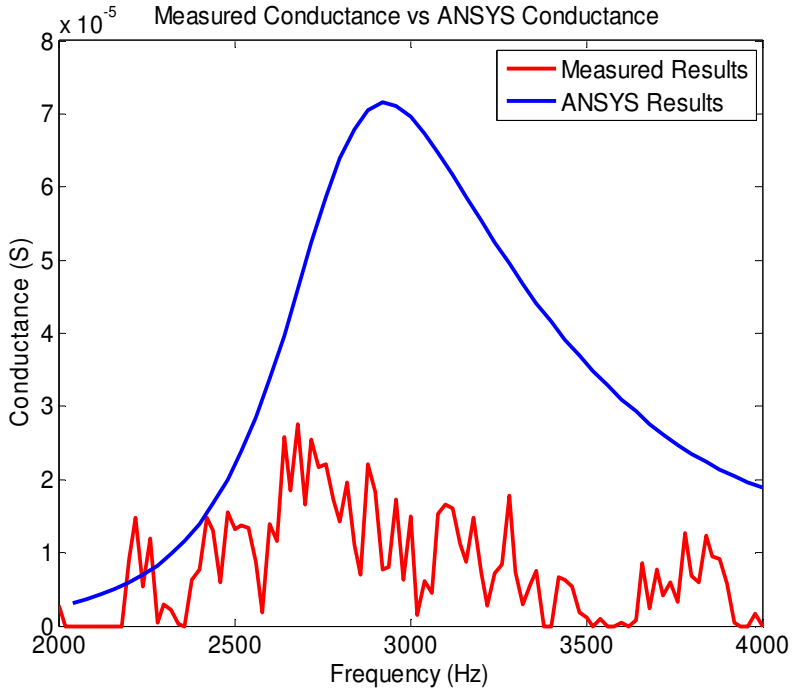

Figure 55 In-water conductance measured in water tank vs. conductance obtained in ANSYS

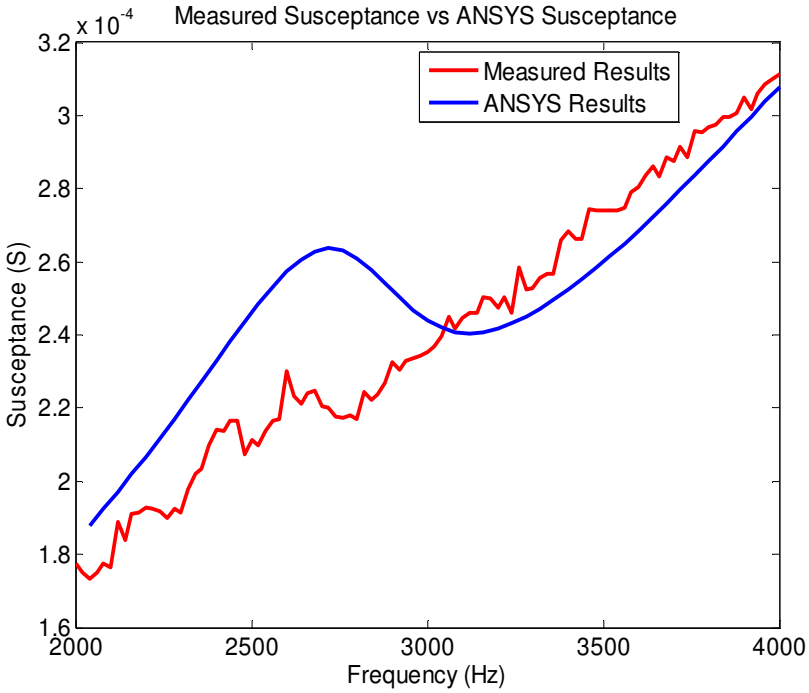

Figure 56 In-water susceptance measured in water tank vs. susceptance obtained in ANSYS

Conductance and susceptance plot obtained by water tank measurements illustrates that reflections affect the results significantly. Therefore, interpreting and comparing the measured results with theoretical results obtained in ANSYS are insignificant in terms of the performance of transducer.

We have repeated the in-water admittance measurement of transducer in water-reservoir inside the Bilkent University between the Main Campus and East Campus as shown in Figure 57. We placed the measurement set up consisting LCR-8101 impedance analyzer, laptop, 2 x $12V_{dc}$ accumulators and 1 x 24V-$220V_{ac}$ inverter to feed the electronic equipments. We have taken the measurement where the depth is 3m and distance from the shore is 5m. The bottom of the reservoir is mud that has low reflectivity. Figure 58 and Figure 59 illustrates the comparison of ANSYS and measured in-water conductance and susceptance of transducer taken in reservoir, respectively.

Figure 57 Reservoir inside Bilkent University

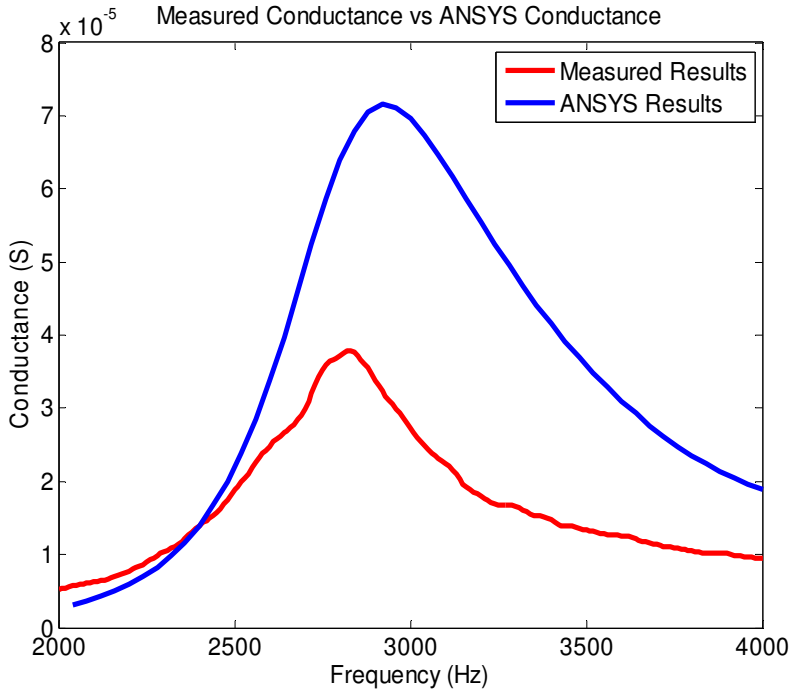

Figure 58 In-water conductance measured in reservoir vs. conductance obtained in ANSYS

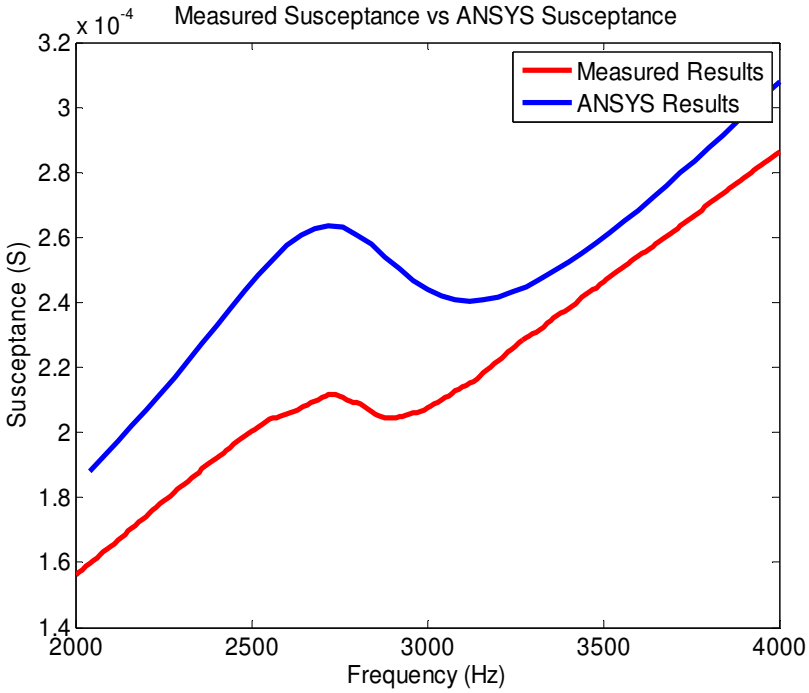

Figure 59 In-water susceptance measured in reservoir vs. susceptance obtained in ANSYS

We have reduced the effects of reflection and greatly increased the reliability of measurements by conducting the measurements in reservoir. We obtain the 2.82 kHz measured resonance frequency where the theoretical resonance frequency is 2.92 kHz. However, measured conductance at resonance frequency is 38 μS where the theoretical conductance at resonance frequency is 72 μS. Conductance of transducer is proportional with the square of the piezoelectric constant, d_{33}, as ;

$$G \propto (d_{33})^2 \tag{7.5}$$

Ratio of measured conductance and theoretical conductance is;

$$\frac{G_{measured}}{G_{theoratical}} = \frac{38\mu S}{72\mu S} \cong 0.53 \tag{7.6}$$

Therefore, the ratio of the piezoelectric coefficient with the one we use in theoretical calculations is the square root of the value obtained in Eq. 7.6 , which is 0.73.

$$\frac{d_{33measurement}}{d_{33datasheet}} = \sqrt{0.53} = 0.73 \tag{7.7}$$

Piezoelectric rings that we have used are more than twenty years and change in the piezoelectric coefficient found as in Eq. 7.7 is reasonable. Other possibility is that the original piezoelectric coefficient value of those rings might be lower than the present piezoelectric coefficient value.

Blocked capacitance, C_b, of transducer is calculated as

$$C_b = \frac{B}{2\pi f_0} \tag{7.8}$$

where B is susceptance at resonance frequency and f_0 is the resonance frequency.

The theoretical and experimental results are summarized in Table 7.

Parameter	Theoretical Results	Experimental Results
$\mathbf{f_{0,air}}$	5 kHz	4.73 kHz
$\mathbf{f_{0,water}}$	2.92 kHz	2.82 kHz
$\mathbf{BW_{water}}$	880 Hz	215 Hz
$\mathbf{Q_{water}}$	3.32	4.3
$\mathbf{G_{max}}$	72 μS	38 μS
$\mathbf{C_b}$	13.6 nF	11.7 nF

Table 7 Theoretical Results vs. Measured Results

Chapter 8

Conclusion

The need for the detection of targets from long distances increases the importance of high power and low frequency transducer. In this thesis, the design of barrel-stave flextensional transducer is reported.

Comparison of the equivalent circuit results of barrel-stave transducer with the Bayliss's FEM results illustrated the inconsistency between the FEM and equivalent circuit results, so design of transducer is done using FEM.

The finite element method is used to investigate the electro-acoustic behavior of barrel-stave transducer with high accuracy, although computationally intensive.

Among eight design parameters of barrel-stave transducer, we have optimized the transducer performance with low Q-factor using five structural parameters which are; radius of curvature of shell profile, r, shell thickness, t, length of device between end plates, l, radius at end of device, r_e, thickness of end plate, h_p. We have used the PZT-4 rings that we have in hand, so we were somewhat limited in design.

Low frequency and low quality factor requirement is accomplished with D3 design parameter set given in Table 5. We have acquired much lower quality factor and relatively larger power level compared to the scaled version of Bayliss's slotted-shell design.

Thereafter, some of equivalent circuit elements are modified using the FEM results and it is illustrated that the modified circuit results are compatible with the FEM results.

Power limitations of barrel-stave flextensional transducer are examined in terms of electrical limitations, cavitation, and thermal limitations. Cavitation and thermal analysis are carried out by applying the voltage creating the electric field limit of 2000 V/cm. Cavitation threshold limits the power up to a depth of 33 meters. Thermal analysis is carried out for various combinations including the coating of transducer and we have found that our design is not a thermally power limited. Consequently; up to 33 meters, cavitation limits the acoustic power of barrel-stave transducer and after this depth, maximum electric field applied to ceramic materials before depolarization limits the acoustic power.

Vacuum measurements agree well with the FEM results; however, we face some difficulties in in-water measurements. Water tank is small compared to our desired amount of wavelengths in order not to take reflections. Therefore, conductance and susceptance plot obtained by water tank measurements illustrates that reflections affect the results significantly. We have repeated the in-water measurements of transducer in water-reservoir inside the Bilkent University and reduced the effects of reflection and greatly increased the reliability of measurements.

As a future work, more experimental work would be to carry out to obtain the entire acoustic characteristics of transducer. In addition, array formation using barrel-stave flextensional transducer could be studied.

Appendix I

The 'base' values of the structure's dimensions and the material properties

Parameter	Description	Base Value
r	Radius of curvature of shell profile	0.25m
t	Shell thickness	15mm
l	Length of device between end plates	25cm
r_e	Radius at end of device	85mm
h_p	Thickness of end plate	30mm
r_i	Inner radius of the ceramic stack	20mm
ro	Outer radius of the ceramic stack	40mm
n	Number of staves forming the shell	12

Table 8 Structural parameters and their base values

Part	Material	Density (kg m-3)	Young's modulus (GPa)	Poisson's ratio
Ceramic	PZT-4			
Insulator	MACOR	2520	140.0	0.29
End-plate	Steel	7960	193.0	0.31
Shell	Aluminum	2710	68.91	0.30
Glue joints	Araldite	1180	6.5	0.40

Table 9 Material Properties used in Clive Bayliss Thesis

Part	Material	Density (kg m-3)	Young's modulus (GPa)	Poisson's ratio
Shell	Carbon/Fiber Epoxy	1800	225	0.33
Insulator	%96 Alumina	3800	300	0.22

Table 10 Carbon/Fiber Epoxy and Alumina Material Properties

Appendix II

Effective Vibrating Mass of Stack

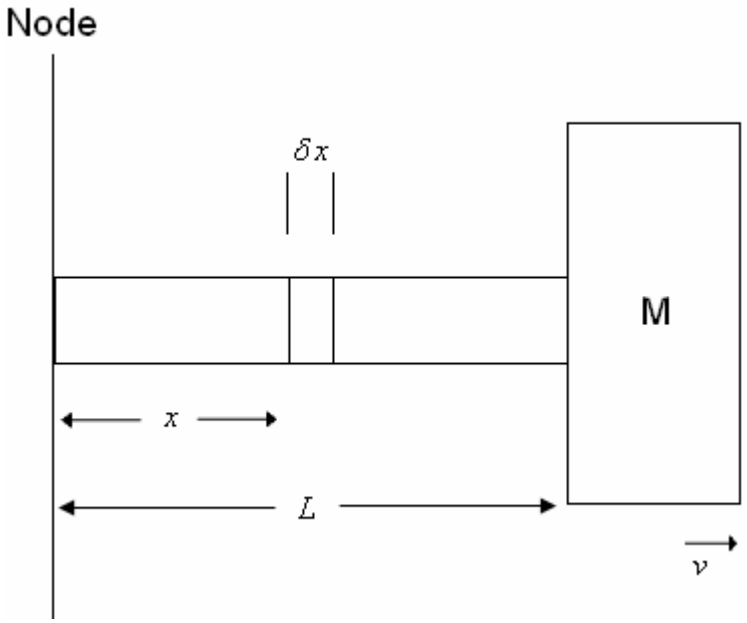

Figure 60 Basic static and end mass

Figure 60 shows the basic static and end mass configuration of transducer. Assume that the displacement of the stack is approximately proportional to its distance from the nodal plane. The displacement velocity of the element δx at a distance x from the node is approximately vx/L, where L is the total length of the stack and v is the velocity of the end mass M. When the static mass of the static mass of the stack is M_s, the mass of the element is $M_s \delta x / L$. The kinetic energy of the system is written as;

$$E_k = \frac{1}{2}\left(Mv^2 + \int_0^L \frac{M_s}{L} dx \frac{(vx)^2}{L^2} \right) \qquad \text{(II-1)}$$

$$E_k = \frac{1}{2}\left(Mv^2 + \frac{M_s}{L}\frac{v^2}{L^2}\frac{L^3}{3} \right) \tag{II-2}$$

$$E_k = \frac{1}{2}\left(Mv^2 + \frac{M_s v^2}{3} \right) \tag{II-3}$$

$$E_k = \frac{1}{2}\left(M + \frac{M_s}{3} \right) v^2 \tag{II-4}$$

Therefore, the effective vibrating mass of the stack is $M_s/3$, which is added to the end masses in the equivalent circuit equations [3].

Appendix III

Element Types Used in the ANSYS Model

Element type entry window in ANSYS is illustrated in Figure 61.

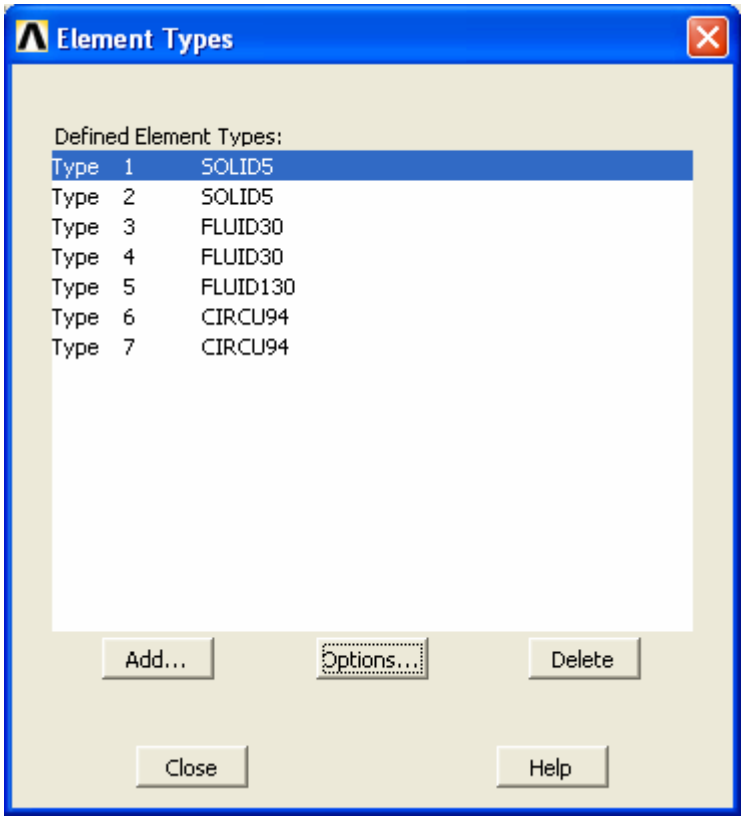

Figure 61 Element type selection window in ANSYS

Material Matrices for PZT-4

Density of PZT-4 element is;

$$\rho = 7500\, kg / m^3$$

For +Z and –Z polarized PZT-4 rings Dielectric matrix, and Stiffness matrix coefficients are the same and given as;

PZT-4 Dielectric Matrix [ε_r]:

$$\begin{bmatrix} 730 & 0 & 0 \\ 0 & 730 & 0 \\ 0 & 0 & 635 \end{bmatrix}$$

PZT-4 Stiffness matrix [c] x GPa

$$\begin{bmatrix} 139 & 77.8 & 74.3 & 0 & 0 & 0 \\ & 139 & 74.3 & 0 & 0 & 0 \\ & & 115 & 0 & 0 & 0 \\ & & & 30.6 & 0 & 0 \\ & & & & 25.6 & 0 \\ & & & & & 25.6 \end{bmatrix}$$

PZT-4 Piezoelectric Matrix coefficients change its sign as it changes its polarization direction from +Z to –Z direction as;

+Z polarized PZT-4 Piezoelectric Matrix [e] C/m^2

$$\begin{bmatrix} 0 & 0 & -5.2 \\ 0 & 0 & -5.2 \\ 0 & 0 & 15.1 \\ 0 & 0 & 0 \\ 0 & 12.7 & 0 \\ 12.7 & 0 & 0 \end{bmatrix}$$

-Z polarized PZT-4 Piezoelectric Matrix [e] C/m^2

$$\begin{bmatrix} 0 & 0 & 5.2 \\ 0 & 0 & 5.2 \\ 0 & 0 & -15.1 \\ 0 & 0 & 0 \\ 0 & -12.7 & 0 \\ -12.7 & 0 & 0 \end{bmatrix}$$

Appendix IV

Thermal Properties of Materials

Thermal properties of materials that are used in thermal analysis are given in Table 11.

Material	Thermal Property	Value	Unit
PZT-4	Thermal Conductivity	1.8	W/m°K
	Specific Heat	3192000	J/m^3°K
Steel	Thermal Conductivity	54	W/m°K
	Specific Heat	3744000	J/m^3°K
Aluminum	Thermal Conductivity	237	W/m°K
	Specific Heat	2422000	J/m^3°K
Epoxy	Thermal Conductivity	0.2	W/m°K
	Specific Heat	2562000	J/m^3°K
Polyurethane	Thermal Conductivity	0.2	W/m°K
	Specific Heat	88000	J/m^3°K
Water	Convection Coefficient	1350	W/m^2°K
Air	Convection Coefficient	22	W/m^2°K

Table 11 Thermal properties of materials

Appendix V

Construction Details of Barrel-Stave Transducer

The cross-section view of transducer is illustrated in the first drawing.

Components

8 x PZT-4 rings

8 x Aluminum Stave

1 x Stainless Steel Endplate without holes (Endplate I)

1 x Stainless Steel Endplate with 2 holes (Endplate II)

2 x Alumina Insulator

2 x Stainless Steel Washer

9 x Copper Berilium Conductor Sheet

1 x Stainless Steel Center Bolt

Adhesives

Ecobond 45 Clear and Catalyst 15 Clear mixed 1:1 ratio for rigid gluing and applied between PZT rings, conductor sheets, insulators and washers (Emerson & Cuming)

We have applied epoxy / polyamide adhesive with ratio of 1:1 between the endplates and aluminum staves. The adhesive is the product of Tyco Raychem with type number of S1125-KIT-8.

Other Materials

16 x (M4x10) cross necessed countersunk (flat) head screw

3 x M10 Hexagon Nut

Single core silicon insulated cable with1500V rating.

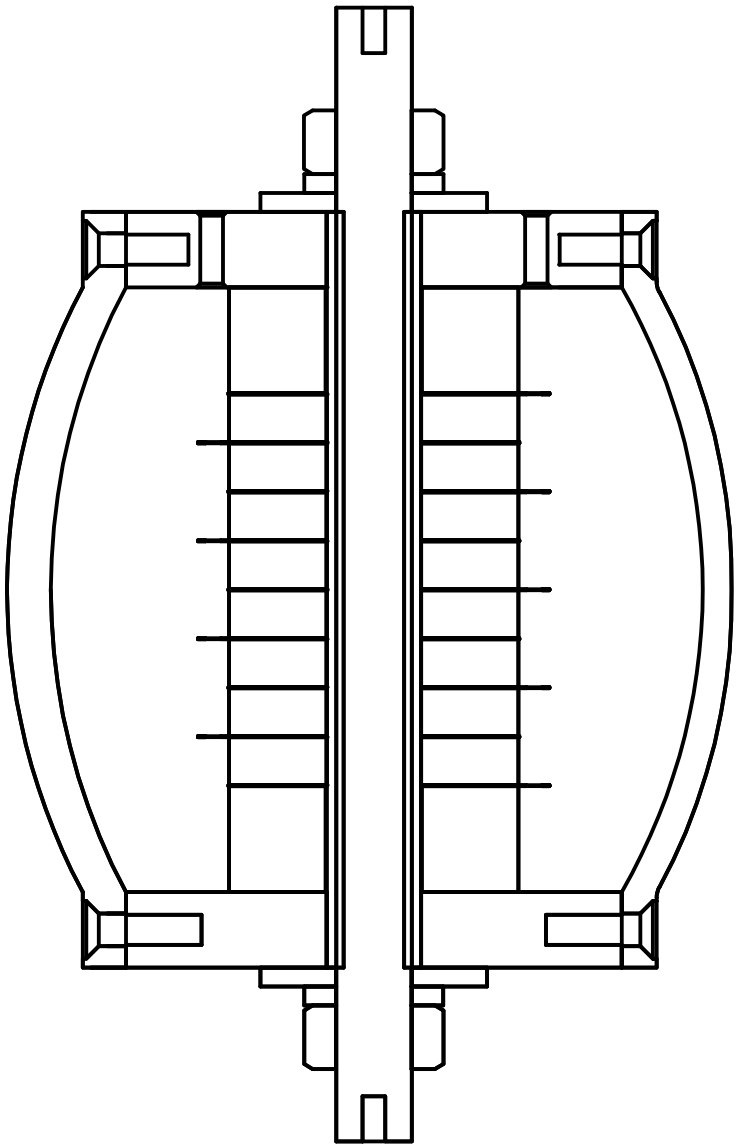

BARREL -STAVE FLEXTENSIONAL TRANSDUCER ASSEMBLY	CROSS-SECTION VIEW	DATE: 02/02/2009
	SCALE 1:1	Size A4

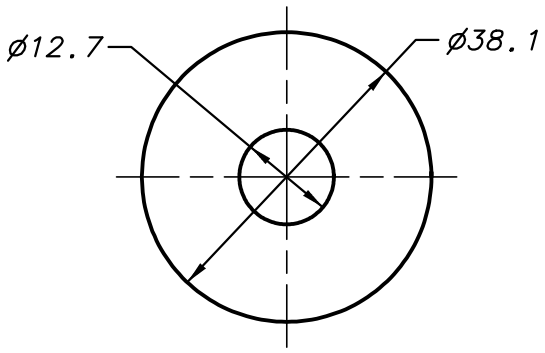

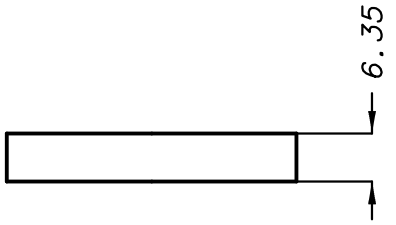

BARREL-STAVE FLEXTENSIONAL TRANSDUCER PZT-4 RING	DIMENSIONS IN MILLIMETERS		DATE: 02/02/2009
	SCALE 1:1	MATERIAL PIEZOELECTRIC	Size A4

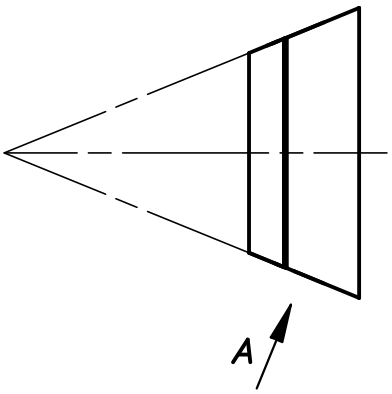

VIEW A

SCALE 1:1

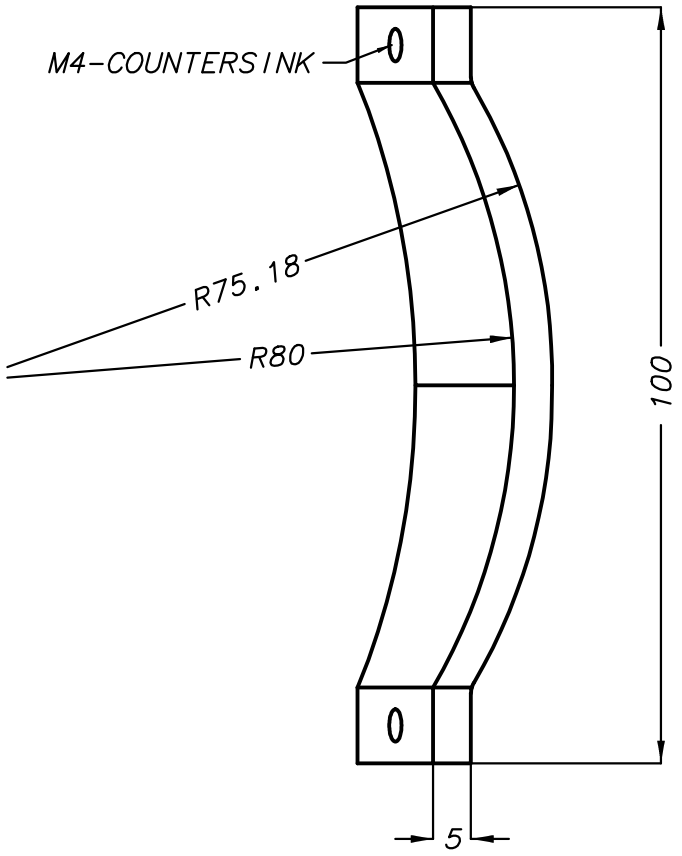

BARREL-STAVE FLEXTENSIONAL TRANSDUCER STAVE	DIMENSIONS IN MILLIMETERS		DATE: 02/02/2009
	SCALE 1:1	MATERIAL ALUMINIUM	Size A4

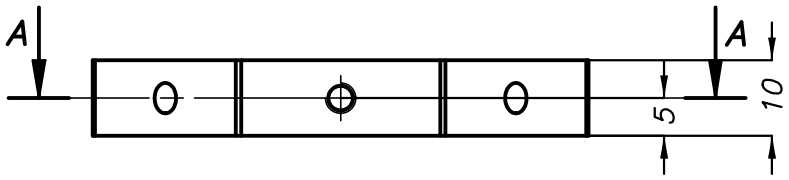

SECTION A-A

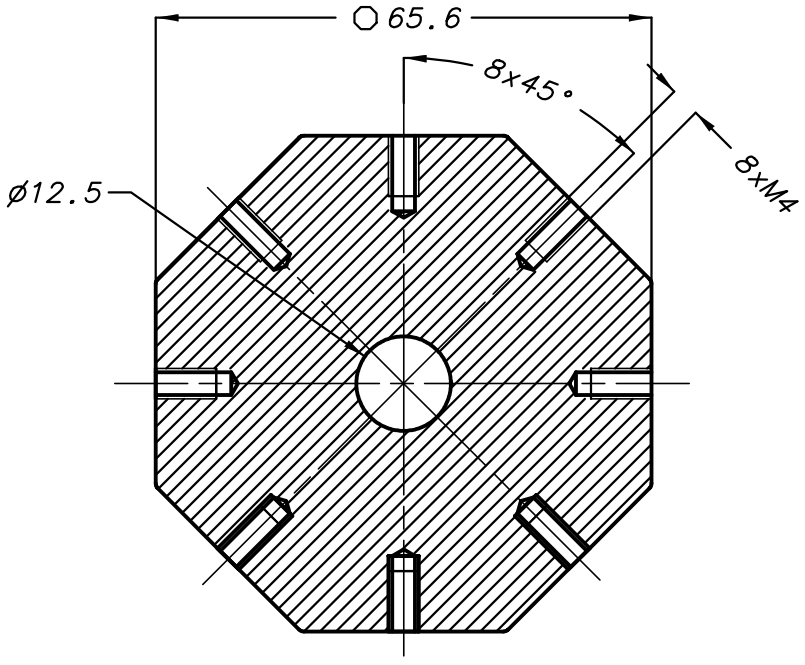

BARREL-STAVE FLEXTENSIONAL TRANSDUCER ENDPLATE I	DIMENSIONS IN MILLIMETERS		DATE: 02/02/2009
	SCALE 1:1	MATERIAL STAINLESS STELL	Size A4

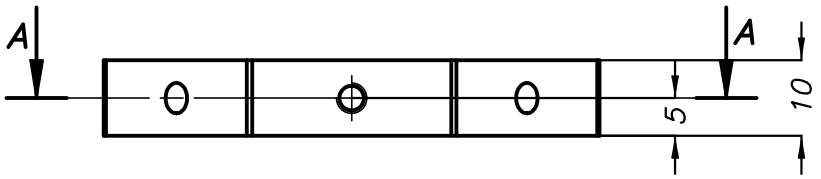

SECTION A-A

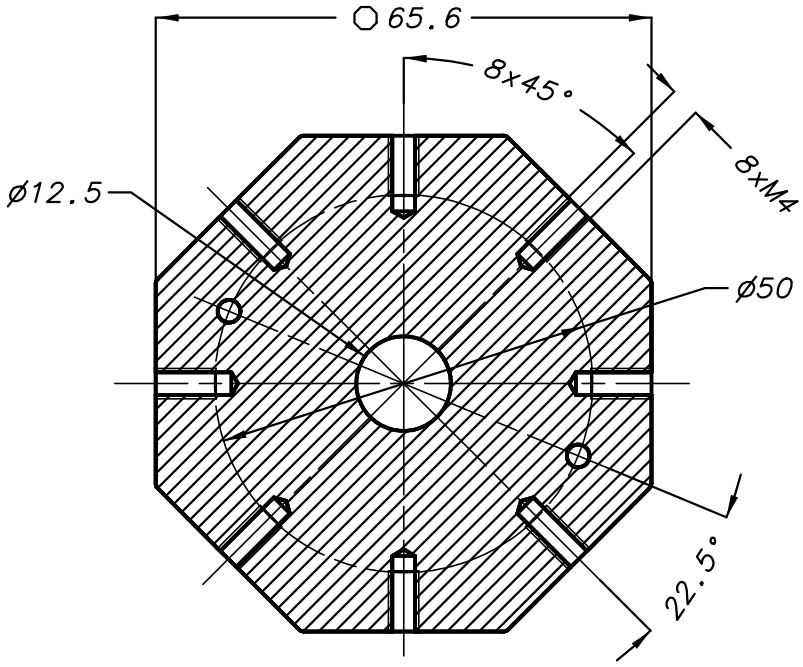

BARREL-STAVE FLEXTENSIONAL TRANSDUCER ENDPLATE II	DIMENSIONS IN MILLIMETERS		DATE: 02/02/2009
	SCALE 1:1	MATERIAL STAINLESS STEEL	Size A4

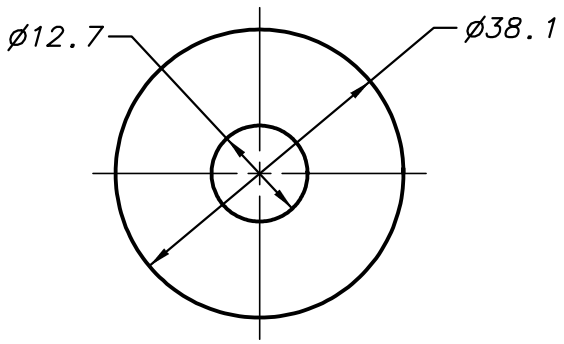

BARREL-STAVE FLEXTENSIONAL TRANSDUCER INSULATOR	DIMENSIONS IN MILLIMETERS		DATE: 02/02/2009
	SCALE 1:1	MATERIAL ALUMINA	Size A4

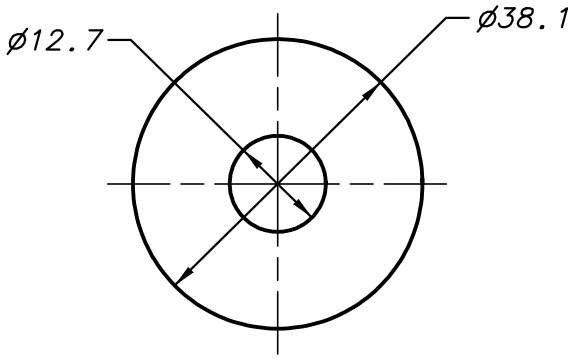

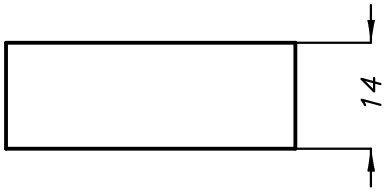

BARREL-STAVE FLEXTENSIONAL TRANSDUCER WASHER	DIMENSIONS IN MILLIMETERS		DATE: 02/02/2009
	SCALE 1:1	MATERIAL STAINLESS STEEL	Size A4

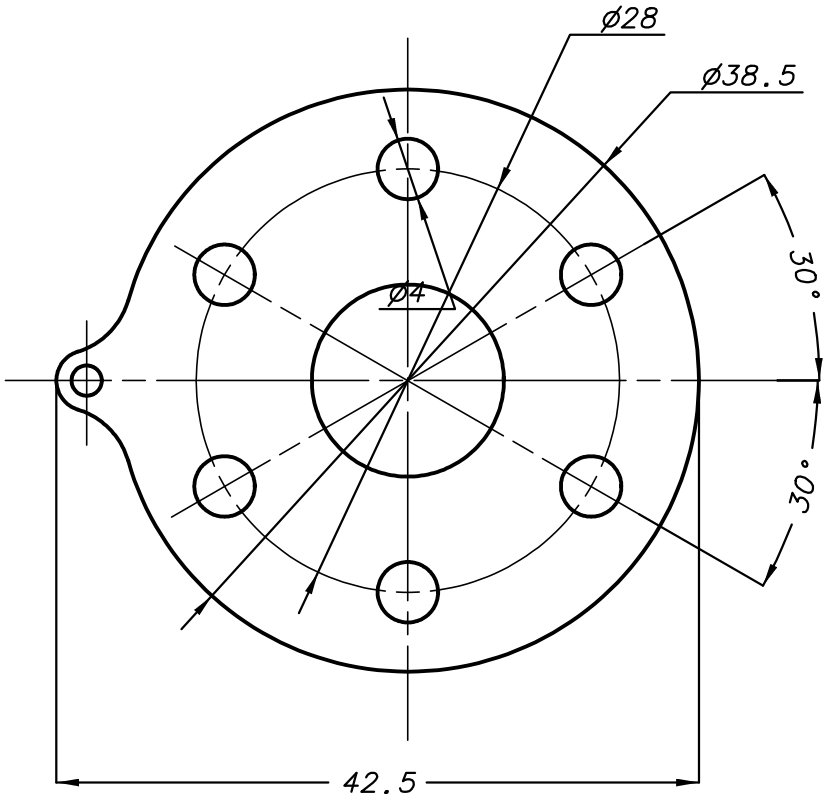

BARREL-STAVE FLEXTENSIONAL TRANSDUCER CONDUCTOR SHEET	DIMENSIONS IN MILLIMETERS	DATE: 02/02/2009
	SCALE 1:1 / MATERIAL COPPER BERILIUM	Size A4

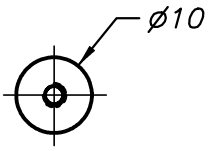

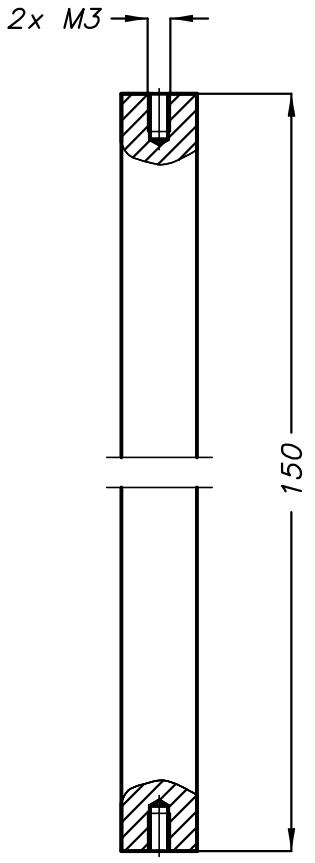

BARREL-STAVE FLEXTENSIONAL TRANSDUCER CENTER BOLT	DIMENSIONS IN MILLIMETERS		DATE: 02/02/2009
	SCALE 1:1	MATERIAL STAINLESS STEEL	Size A4

Appendix VI

Measured Results for Transducer constructed with Petrolatum

Transducer structure is tested in two steps before applying glue to components in order to find out if there is an inconsistency between the theoretical and measured results.

The in-air measured admittance of transducer without aluminum staves is obtained as in Figure 62. Measured resonance frequency is 9.5 kHz and the numerical resonance occurs at 10.7 kHz.

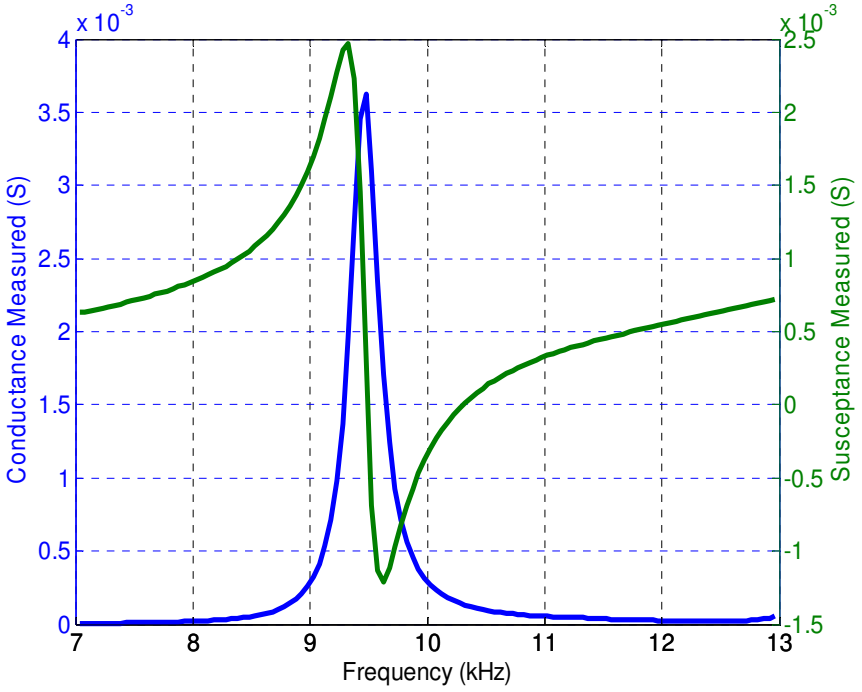

Figure 62 Measured in-air input admittance of transducer without aluminum staves

The in-air measured admittance of transducer with aluminum staves is obtained as in Figure 63. Measured resonance frequency is 4.12 kHz and the numerical resonance frequency is 5 kHz.

We have obtained lower resonance frequency for both measurements. ANSYS model simulates the contacts between the mechanical elements of transducer as strictly bonded, which are proper for the glued case. However, in this case we have used vaseline instead of glue, which decreases the stiffness of transducer structure and also decreases the resonance frequency.

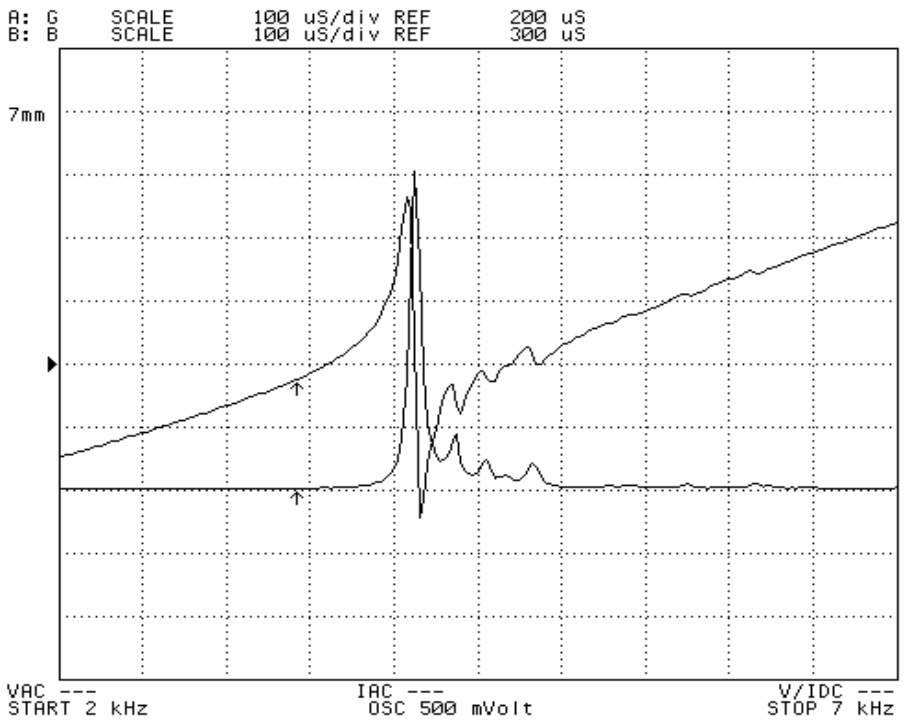

Figure 63 Measured in-air input admittance of transducer with aluminum staves

BIBLIOGRAPHY

[1] X. Lurton, *An Introduction to Underwater Acoustics Principles and Applications.* Springer, 2002

[2] Robert J. Urick, *Principles of Underwater Sound 3rd Edition.* McGraw-Hill Book Company, 1983.

[3] D. Stansfield, *Underwater Electroacoustic Transducers*. Bath, UK: Bath Univ. Press, 1990.

[4] Charles H. Sherman and John L. Butler, *Transducers and Arrays for Underwater Sound.* Springer, 2007.

[5] James R. Phillips, "Piezoelectric Technology Primer"

[6] ANSYS, *Piezoelectrics*, Release 11.0 Documentation for ANSYS, 11.3.

[7] Clive Bayliss, *Application and Development of Finite Element Techniques for Transducer Design and Analysis*, University of Birmingham, 1998.

[8] *Meet the Finite Element Method*, media.wiley.com/product_data/excerpt/89/04713707/0471370789.pdf

[9] D. Roylance, *Finite Element Analysis*, Massachusetts Institute of Technology, 2001.

[10] V. Piefort, A. Preumont, *Finite Element Modeling of Piezoelectric Structures*, Active Structures Laboratory.

[11] William S. Burdic, *Underwater Acoustic System Analysis*. Prentice-Hall, 1990

[12] D.F. Jones, *Flextensional Barrel-Stave Projectors*, in Transducers for Sonics and Ultrasonics, ed. By M.D. McCollum, B.F. Hamonic, and O.B. Wilson, Technomic Publishing Co, 1993.

[13] J.N. Decarpigny , B. Hamonic and O.B. Wilson, *The Design of Low-Frequency Underwater Acoustic Projectors: Present Status and Future Trends,* IEEE Journal Of Oceanic Engineering, Vol. 16, No. I . , 1991

[14] D.T.I. Francis, C. Bayliss, J.A. Ahmad and R.F.W. Coates, *The Development of a Low Frequency Barrel-Stave Transducer for Tomographic Applications Using Finite Element and Boundary Element Modelling*, IEEE 0-7803-2056-5, 1994

[15] M.B. Moffett, J.F.Lindberg, E.A. McLaughlin and J.M. Powers, *An equivalent circuit model for barrel stave flextensional transducers*, in Transducers for Sonics and Ultrasonics, ed. By M.D. McCollum, B.F. Hamonic, and O.B. Wilson, Technomic Publishing Co, 1993.

[16] ANSYS, Release 11.0 Documentation for ANSYS. ANSYS Inc.

[17] David T. Blackstock, *Fundamentals of Physical Acoustics,* Wiley-Interscience Publication, 2000.

[18] *Properties of Piezoelectric Ceramics,* www.morgan-electroceramics.com

[19] Zekeriyya Şahin, *The Design Of A Wideband And Widebeam Piston Transducer In A Finite Closed Circular Baffle*, Bilkent University, 2008